Helsinki University of Technology
CFD-group/ The Laboratory of Applied Thermodynamics

MEMO No CFD/THERMO-23-97 DATE: November 17, 1997

TITLE

Flow Simulation of a Centrifugal Process Pump

AUTHOR(S)
Juha Ojala

ABSTRACT

The main object of these calculations is the industrial evaluation of a FINFLO flow solver using a low-Reynolds number $k-\epsilon$ and Reynolds stress turbulence models with a rotation correction. The results from the $k-\epsilon$ simulations are good whereas the Reynolds stress model has problems in numerical stability and convergence.

MAIN RESULT

A pump grid for low-Reynolds number turbulence models was made. After that various cases were simulated using a Reynolds Stress model and a low-Reynolds number $k-\epsilon$ turbulence model with a rotation correction.

PAGES
47

KEY WORDS
FINFLO, centrifugal pump, $k-\epsilon$-model, Reynolds stress model (RSM), rotation correction, pump head and efficiency.

APPROVED BY

Timo Siikonen November 17, 1997

1 Introduction

A centrifugal process pump made by Ahlström is calculated for industrial evaluation purposes of a FINFLO [1] flow solver. Two turbulence models, Chien's low-Reynolds number $k-\epsilon$ model [2] and the Reynolds stress model (RSM) by Speziale, Sarkar and Gatski (SSG) [3] have been used. The $k-\epsilon$ model has a rotation correction. Also the RSM model have coriolis force terms for the Reynolds stresses.

FINFLO is a finite-volume CFD program for complex three-dimensional geometries. The program utilizes Cartesian velocity components in a cell-centred approach. The discretized equations are integrated in time by applying an implicit method. A multigrid V-cycle is applied for acceleration of converence. The main features of the numerical methods of the code are described in [4].

2 Process Pump

The present process pump is a water pump with five blades. The outer diameter of the impeller is 416 mm and the angular velocity is 1485 rpm. The total volume flow at a design point is 264.3 l/s. These values give a static head of about 35 meters (over the whole pump), while the mechanical power required is about 135 kW. The impeller is half open, i.e. the hub is rotating with the impeller whereas the shroud does not rotate.

3 Grid

The grid generation was started from the geometry data given in IGES-format (Fig. 1). The

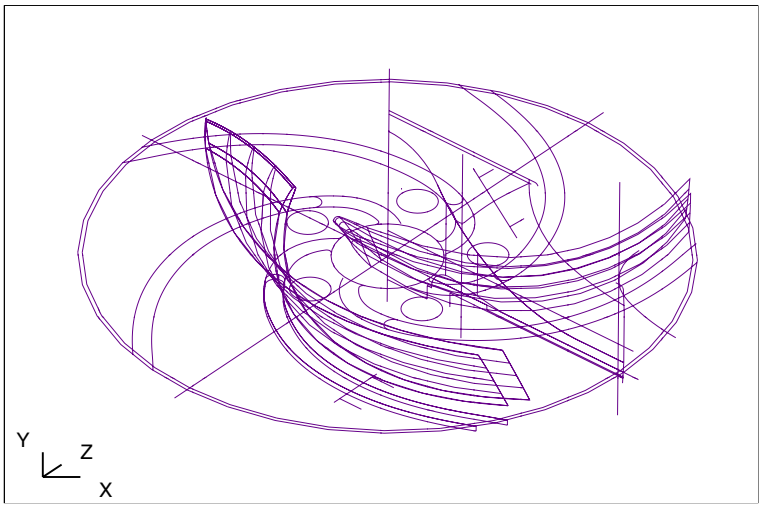

Fig. 1: The pump geometry as IGES-data.

data format is supported by the IGG [5] and so it was easy to read it into the grid generator. The first task was to make surface grids of the blades (Fig. 2).

After the IGES-data was read into the program, all unnecessary data was removed. Only the blade surface was retained. Then a quite dense grid was interpolated on the blade. Because the H-type grids were used, the pressure and suction sides had to be distinguished at the leading edge. After that we had the pressure and suction sides, but the clustering near the walls was not necessarily good.

When using the H-type grids, the most common practise is to make the volume grid by rotating a face from blade to blade. The starting point in that case is that the both faces are available. Also all the clustering near the walls has to be defined. The destination face

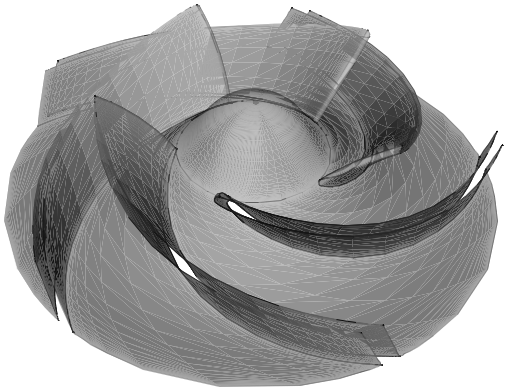

Fig. 2: The impeller surfaces.

should also be rotated 72 degrees and extented because of numerical aspects. After that both faces were completed. Next the volume grid was generated by rotating the source face towards the destination face. The rotation stopped when the source face intersected the destination face.

The H-type grid generation by rotating is almost the only way to generate positive grids in this case. The positive grids can only be achieved by trial and error, one can never know whether is it easier to rotate from a pressure side to a suction side or vice versa. After the volume grid between the blades is positive and the clustering is acceptable, the most difficult phase is over. There still remains many problems, but they are secondary. After the grid between the blades was ready, the blocks before them were generated. The block which turns the axial flow to the blades was generated by linear interpolation and rotation. At first the volume grid was generated by a 6-wall interpolation, but this approach failed. The positive grid was achieved by generating inner points using rotation. The straight block above the previous one was generated by translating the connection surface in the direction of the rotation axis.

The diffuser block was modelled in this case as vaneless. That is not actually true, but no information about the diffuser was available. The diffuser was made by extruding the impeller outlet radius until it was 350 mm.

The whole grid (Fig. 3) consists of four calculational blocks and two boundary blocks, one inlet and one outlet block. The number of cells in calculation blocks is

```
IDMN(  1) =  65, JDMN(  1) =  33, KDMN(  1) =  65
IDMN(  2) =  65, JDMN(  2) =  65, KDMN(  2) =  65
IDMN(  3) = 129, JDMN(  3) =  65, KDMN(  3) =  65
IDMN(  4) =  33, JDMN(  4) =  65, KDMN(  4) =  97

NCELL =      1114112
```

Input and output blocks were generated by Rautaheimo's inoutblock-grid generator [1].

The autogrid option of the IGG [5] was also tested. It succeeded in the cascade grid generation, but the problem was the rotation axis because of singularity. The supplier of the IGG, Numeca has promised that the next version should also work in this case. The main conclusion of the autogrid is that it can make grids for Euler or high-Reynolds number turbulence models with wall functions. When low-Reynolds number models are used, the clustering near the walls cannot be made dense enough. If the height of the first cell was set to $4 \cdot 10^{-6}\, m$, which means that y^+ is almost one, the autogrid made a grid that had cells with negative volumes. So the present version of autogrid is not capable of making good grids for low-Reynolds number turbulence models.

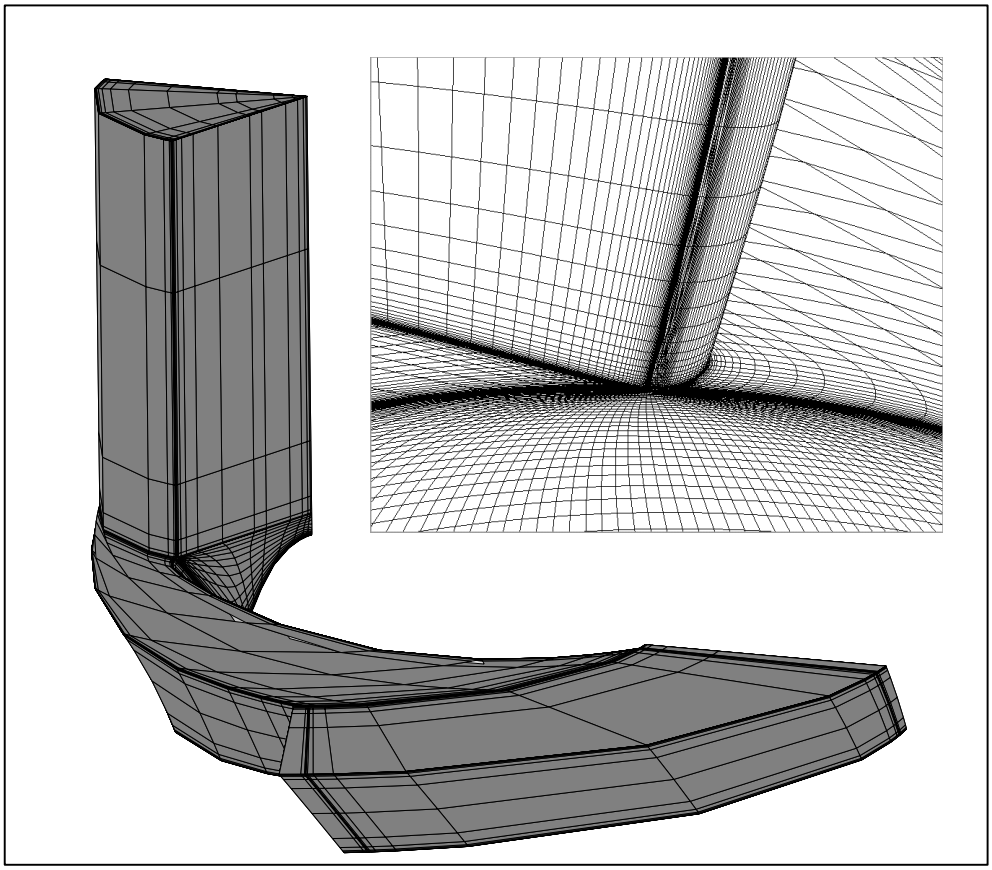

Fig. 3: The whole grid (grid level 3) and detail from the leading edge (level 1).

4 Turbulence Models

All the flow cases are calculated using the FINFLO flow solver [1]. It is a multi-block Navier-Stokes solver that uses structural grids. There any many turbulence models available, and in this project the Chien's low-Reynolds number $k-\epsilon$-model has been used with a rotation correction. Also some test calculations with the SSG-Reynolds stress model were performed. That turbulence model is a very complicated state-of-the-art model. It has been previously used only in simple test cases and the tests performed in this project are the most complicated that the author has seen.

4.0.1 Low Reynolds Number $k-\epsilon$ Model

Chien's $k-\epsilon$-model [2] is a low-Reynolds number version of the most popular turbulence model in industrial applications. The standard $k-\epsilon$ model is not a low Reynolds number model. This means that by using that standard model one have to use wall-fuctions near the wall (in the low-Reynolds number region). The wall functions assume universal conditions there. Because the near wall flow in a pump is very complicated and great pressure gradients exists, error in near wall flow will occur if wall-functions are used. By using low-Reynolds number model, the equations for k and ϵ are used to the wall. Only wall damping have to be employed. With a low-Reynolds number model the near wall flow should be better simulated than with a high Reynolds number model. The differences in global pump parameters (head, power and so on) can be, nevertheless, quite small in practise.

The standard $k-\epsilon$-model does not take coriolis and centrifugal forces into account in turbulence equations. Because of that asymmetric distributions of turbulence quantities

cannot be predicted correctly. Many rotation corrections have been published in the literature and some of them have also been tested in FINFLO (see ref. [6]). The best of tested corrections is implemented in FINFLO and it is also used in this work. In that correction the dissipation equation is

$$\frac{\partial}{\partial x}(\rho u\epsilon) + \frac{\partial}{\partial y}(\rho v\epsilon) = \frac{\partial}{\partial x}\left(\frac{\mu_t}{\sigma_\epsilon}\frac{\partial \epsilon}{\partial x}\right) + \frac{\partial}{\partial y}\left(\frac{\mu_t}{\sigma_\epsilon}\frac{\partial \epsilon}{\partial y}\right) + C_1\epsilon P/k - C_2(1+C_c)\rho\epsilon^2/k$$

where

$$C_c = -0.2Ri$$

and

$$Ri = -\omega\left(s-\omega\right) \tag{1}$$

where ω is a nondimensional vorticity and s is a nondimensional strain rate. The modification of the dissipation equation is made according to Howard [7] and the Richardson number is calculated according to Khodak et al. [8]. For further information, see refs. [6], [7] and [8].

4.0.2 Reynolds Stress Model

The Reynolds-stress model (RSM) can be written in the following form

$$\frac{\partial \bar{\rho}\widetilde{u_i'' u_j''}}{\partial t} + \frac{\partial(\bar{\rho}\tilde{u}_k\widetilde{u_i'' u_j''})}{\partial x_k} = P_{ij} - \Omega_k\left(\bar{\rho}\widetilde{u_j'' u_m''}\epsilon_{ikm} + \bar{\rho}\widetilde{u_i'' u_m''}\epsilon_{jkm}\right) + \Phi_{ij} + D_{ij} - \epsilon_{ij} \tag{2}$$

where P_{ij}, Φ_{ij}, D_{ij} and ϵ_{ij} are the production term, the pressure-strain term, the diffusion term and the dissipation term, respectively [9]. The second term including the angular velocity of coordinate system, is a term observing coriolis and centifugal forces.

The production term is exact, whereas the turbulent diffusion, the pressure strain and the dissipation rate must be modeled. In this work the low-Reynolds number version of Speziale, Sarkar and Gatski (hereafter referred as SSG) [3] model is used. The low-Reynolds number modeling is based on Shima's work [10]. In the SSG model the low-Reynolds number model is adapted from Shima in a similar way as in [11]. In both cases the dissipation transport equation is based on the Chien's $k-\epsilon$ model [2].

5 Flow Simulation

The main parameters in the flow simulation are set in the INPUT-file. One of the most important parameter, Courant number (CFL) has to be set between 1.0 and 2.0 depending on the case. For a faster convergence two multigrid levels were used. The calculations were started from the third grid level and continued to the second level in Silicon Graphics Indigo^2 R10000 workstation. The calculations at the finest grid level were performed on the Origin 2000 server using two R10000 processors. The size of the first level run was 526.5 Mb. That was devided to 290.3 Mb and 236.3 Mb between processors.

5.1 Convergence

As an example, the head and the L_2-norm of the x-momentum residual convergence are shown in Fig. 4. The pressure field and head converge quite fast, but the turbulence quantities behave more slowly. The x-momentum residual oscillates at the level of 10^{-5}, but the final level seems to be achieved. The peak in the x-momentum at 7000 cycles becames from the changes in the number of multigrid levels. The simulations have been run until the pressure field and the mass flow does not change and also other quantities have achieved their final level.

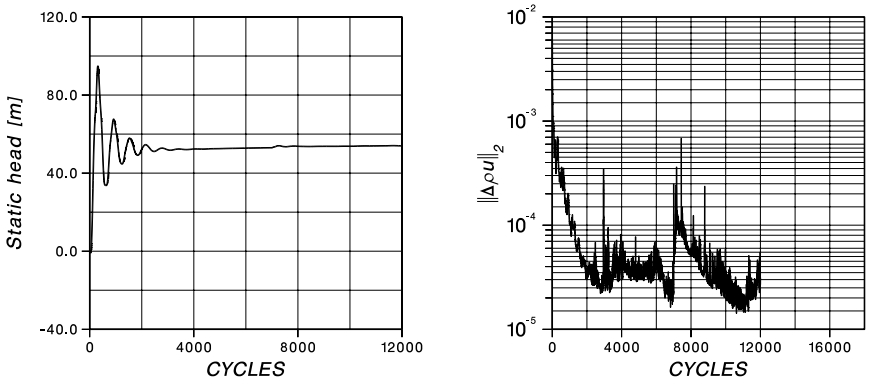

Fig. 4: Two examples of convergence.

6 Results

6.1 Streamlines inside the Impeller

The figures in Appendix A present the general flow field inside the impeller. The figures have been taken from the grid level 2. The massflow in the first figure is 20 % of design point's massflow, the other cases are 40 %, 60 %, 80 %, 100 %, 120 %, 140 % and 160 %. In the first figures (Fig. 7 and Fig. 8) we can see how the flow does not go into the blade passage and massive flow separation occurs. At the massflow of 20 % and 40 % there exists also back flow regions. At the design point (upper part of Fig. 9) the flow behaves well and separation cannot be seen. Also in the case when the massflow is greater than at the design point, the flow seems to go smoothly without separation.

The streamlines near the blade surfaces are shown in the two last figures (Fig. 11) in Appendix A. Those figures have been plotted from the finest grid level at the massflow rate of the design point. Small vorticies can been seen in the both last figures. Also a low momentum area near the pressure side is seen as a blue ribbon.

6.2 Velocity Vectors on the Meridional Plane

The figures in Appendix B show velocity vectors in the center of the passage. Massive back flow regions can be seen in simulations which have been made using low massflow rates. In the design point simulation the flow field is smooth without back flows. The results from level 3 differ quite much from the results from the second level. The simulation on the coarsest level (level 3) cannot predict back flows and other flow features as well as on denser level (level 2). It can also be seen that the grid density has a significant effect on the flow after the blade region even in the case without separation. As expected at the design point (Fig. 16) this difference is the smallest. It can be concluded that the numerical accuracy is more difficult to be obtained in the simulations far from the design point.

The velocity vectors near the pressure and suction side are presented in Appendix C. Only three cases have been printed out, they are at 20 %, 100 % and 160 % massflows. In all cases the flow fields at the pressure side and suction side are quite similar.

6.3 Pressure on Impeller Surfaces

The pressure field on the impeller surfaces are presented in Appendix D and Appendix E. In Appendix D the whole impeller is shown in all massflow cases at grid level 2. Those figures show how the pressure rises smoothly in the design point calculation and there are not any lower or higher pressure areas on the blade surface like in the extreme case where $Q/Q_0 = 160\%$. The pressure difference between the inlet and the outlet is the greatest at

the lowest massflow. The same phenomenon can be better seen from the calculated pump curve (see section 6.6).

Total pressure distributions on the pressure and suction sides are shown in Appendix E. From these figures one can see that the smoothest pressure rise occurs at the design point (Fig. 31). At low massflow rates the pressure distribution on the pressure side has a peak near the blade trailing edge (Fig. 27). At the suction side the pressure rises quite smoothly from the leading edge to the trailing edge. There exists, however, quite large low pressure area near the leading edge (Fig. 27). At very high mass flow rates a low pressure peak can be seen near the pressure side leading edge (Fig. 34). At the suction side the low-pressure area is near the shroud in the middle of the blade.

6.4 Static Pressure Around the Blade

Static pressure around the blade is presented in Appendix F. From those figures one can see how the moment around the rotating axis is formed. Curves have been read from near the hub and shroud. In the figures taken from the design point results, it is interesting to see that the pressure difference between the pressure and suction sides is opposite near the leading edge on the hub side. This means that the flow coming to the passage gives energy to the impeller. That kind of phenomenon is unwanted and some kind of leading edge modification should be made to improve the flow behavior there. The previously descriped phenomenon becomes more evident when the mass flow rate is risen. On the basis of the discussion above one can say that the mass flow at optimum operation point may be a little less than the mass flow in the design point.

6.5 Total Pressure Distributions at Various Stations

Total pressure distributions at three stations inside the impeller are shown in Appendix G. The first station is near the leading edge, the second one is at the 50 % of chord and the last one is at the trailing edge. The figures in Appendix G are presented in $\theta - x$-coordinate system. The simulation is calculated at the design point and on the second grid level.

The figures show that the distribution differs quite much between the different locations. Near the leading edge the maximum values are near the shroud and on the pressure side (Fig. 39). In the middle of the chord the maximum value is again near the shroud, but now closer to the suction side (Fig. 40). On the passage exit the distribution is quite uniform, however the maximum appears near the pressure side (Fig. 40).

6.6 Head

Static head is one of the most common parameters in pump design. It is calculated from

$$H_{stat} = \frac{p_2 - p_1}{\rho g} \tag{3}$$

where p_1 is the inlet pressure, p_2 is the outlet pressure, ρ is the density and g is acceleration of the gravity. In this paper two static heads will be presented. The first one is calculated over the hole calculation domain and the other one is calculated over the impeller.

In a left part of the figure 5 the development of the static head in the impeller passage is presented. That result is obtained from grid level 2. At low massflow rates the curve is quite linear but with greater massflow rates the pressure drops after the passage entry. With the greatest mass flow (160 %) this pressure drop is about -15 m. At the lowest massflow rate, there is a rapid rise of pressure near the passage exit.

The pump curve descripes the head as a function of massflow. It is very important for a pump designer and user because it tells much about the characteristics of the pump. To construct a pump curve many cases have to be simulated using different massflows. In this study massflows from 20 % of the massflow of design point to 160 % were used with a 20 %

step. That means 8 different cases. As a result from the second grid level the pump curve in Fig. 5 was constructed.

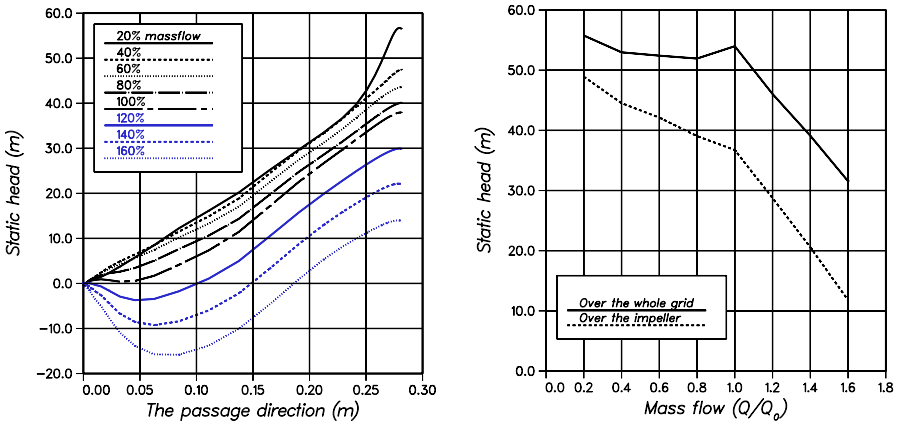

Fig. 5: The static head in the passage and a pump curve (level 2).

The calculated static heads in all cases are presented also in the Table 1. The static head over the whole domain can be read from the left column of Table 1 and the static head over the impeller from the right column of Table 1.

Table. 1: Static head over the whole grid and over the impeller $[m]$.

over the whole grid				over the impeller			
relative	grid level			relative	grid level		
massflow	3	2	1	massflow	3	2	1
20 %	79.4	55.8	-	20 %	70.7	48.9	-
40 %	73.8	53.0	-	40 %	61.7	44.5	-
60 %	69.7	52.4	-	60 %	54.4	42.1	-
80 %	66.6	51.9	-	80 %	48.2	39.0	-
100 %	65.7	54.0	39.3	100 %	44.4	36.7	33.9
120 %	51.1	46.0	-	120 %	27.4	28.7	-
140 %	40.4	39.1	-	140 %	15.4	20.6	-
160 %	28.3	31.6	-	160 %	1.7	11.8	-
RSM	74.1	-	-	RSM	56.6	-	-

At the third grid level all of the head results are too high and the Reynolds stress model gives the highest values. At the grid level 2 the values are smaller and closer the measured value of about 35 m at the design point. It is seen that the head changes when the simulation is performed on the first grid level. This change is more pronounced in the head over the whole grid. Because of this the best head vs. massflow curve could only be obtained from the simulation on the densiest grid level. The grid density is mainly required affected by the low-Reynolds number turbulence models applied.

6.7 Power

The power required by the pump is also one of the most important quantities in pump simulation and design. The following power values (Table 2) have been read from `FINFLO`'s outputfile named `FORCES`. As shown in Table 2, the power needed changes much when the

Table. 2: The power needed ($T\omega$, per cascade) $[kW]$.

relative massflow	grid level 3	2	1
20 %	43.0	24.1	-
40 %	41.7	24.4	-
60 %	41.0	26.5	-
80 %	41.0	29.0	-
100 %	40.3	30.1	25.2
120 %	37.3	29.6	-
140 %	33.4	28.5	-
160 %	27.3	25.6	-
RSM	41.7	-	-

grid level is changed. The third level is much too coarse and for that the results from that grid level are quite uncertain. The results from the second grid level are much better and useful in design as one can see from the design point calculations. That case was calculated also on the densiest grid level and the results did not change very much from the level 2 to the level 1. The Reynolds stress model calculation (RSM) was performed only at the mass flow rate of design point. All the calculated values are shown for one cascade only. So the whole pump values can be obtained by multiplying the table values by the number of blades (5 in this case). For example the needed power at the design point is 150.5 kW ($k-\epsilon$, level 2). That is still about 11 % percent too high. At the finest level the power is about 6.6 % too low, and so the wanted value is between these two values. The mechanical friction losses on the bearings could be about 1 or 2 % of the axial power and the friction losses in the real diffuser and auxiliary parts connecting the pump to the pipe may be also some percents. Also the tip clearence, which was not modeled, causes some losses. So the result from the finest grid level seems to be very good.

6.8 Efficiency and Fluxes of Mechanical Energy

Efficiency is calculated as

$$\eta = \frac{E_2 - E_1}{T\omega} \tag{4}$$

where $E_2 = \dot{V} P_{tot}$ is the mechanical energy flux out, E_1 is the mechanical energy flux in and $T\omega$ is the required axial power. The $\dot{V}$ is the volume flow rate and P_{tot} is the total pressure. The power is presented in the Table 2 and the mechanical energy fluxes into the domain in Table 3. The mechanical energy flux out is shown in Table 4. The left column shows the

Table. 3: Mechanical energy flux to the domain (per cascade) $[kW]$.

relative	grid level		
massflow	3	2	1
20 %	0.22	2.66	-
40 %	1.62	5.95	-
60 %	3.78	9.19	-
80 %	6.48	12.63	-
100 %	8.81	15.03	18.92
120 %	19.95	23.35	-
140 %	31.41	32.84	-
160 %	46.48	44.53	-
RSM	4.35	-	-

flux coming out from the impeller and the right column shows the flux coming out from the whole grid. Finally the efficiency is calculated as a relation of the rise in the mechanical energy flux and the axial power put into the system. The efficiency as a function of massflow

Table. 4: Mechanical energy flux from the impeller and domain (per cascade)$[kW]$.

from the impeller				from the whole domain			
relative	grid level			relative	grid level		
massflow	3	2	1	massflow	3	2	1
20 %	8.52	9.67	-	20 %	11.66	13.63	-
40 %	16.38	17.97	-	40 %	20.14	21.21	-
60 %	23.90	25.75	-	60 %	27.60	28.78	-
80 %	29.88	32.59	-	80 %	34.07	35.86	-
100 %	34.66	38.15	41.96	100 %	38.69	40.17	40.98
120 %	39.08	44.29	-	120 %	43.66	46.95	-
140 %	42.36	49.39	-	140 %	48.06	52.56	-
160 %	44.97	53.93	-	160 %	51.92	57.72	-
RSM	34.45	-	-	RSM	38.57	-	-

is shown in the Fig. 6. From the figure it is seen that the efficiency over the whole grid is lower than the efficiency which was calculated from inlet to the impeller exit. The differences becomes from losses in the modelled diffuser. The shape of the efficiency curve does not change much between these two different efficiency definitions. The maximum value occurs at the design point in both cases and the over the whole domain calculated efficiency is closer to the value read from the manufacturer's data sheet. It is approximately 0.72, i.e. both calculated values are too optimistic. One must, however, remember that the value given by the manufacturer is obtained over the whole pump including a real vaned diffuser, return channel and mechanical friction losses which also reduse the efficiency. Also the difference

between the second and the first grid level efficiencies cannot be forgotten. The best result with the fewest numerical error is obtained from the finest grid level.

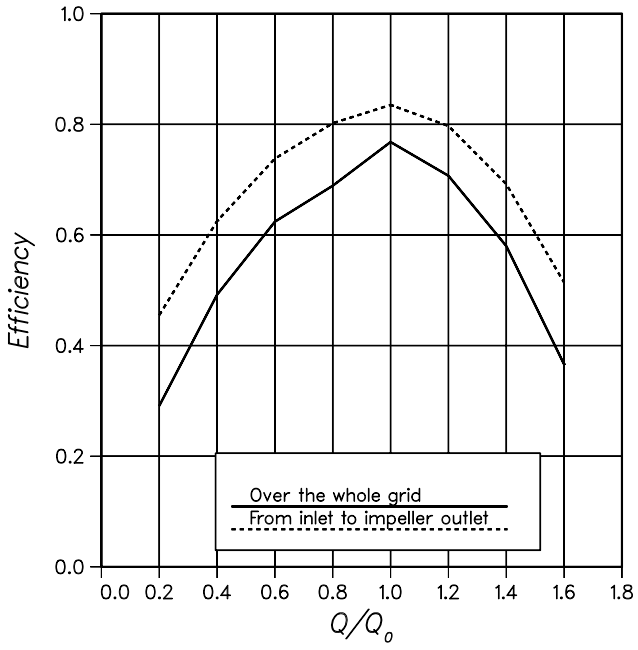

Fig. 6: Efficiency as a function of massflow (level 2).

Table. 5: Efficiency over the whole grid and from inlet to the impeller exit.

relative massflow	grid level 3	2	1	relative massflow	grid level 3	2	1
20 %	0.193	0.291	-	20 %	0.266	0.455	-
40 %	0.354	0.492	-	40 %	0.444	0.625	-
60 %	0.490	0.624	-	60 %	0.581	0.738	-
80 %	0.570	0.689	-	80 %	0.673	0.802	-
100 %	0.641	0.768	0.876	100 %	0.741	0.835	0.915
120 %	0.512	0.707	-	120 %	0.635	0.797	-
140 %	0.328	0.580	-	140 %	0.499	0.692	-
160 %	-0.055	0.366	-	160 %	0.199	0.514	-
RSM	0.721	-	-	RSM	0.820	-	-

The grid level affects quite much on the calculated global quantities. That can be easily seen by reading the power and energy flux tables in this paper. For example when changing the calculation from the grid level 3 to the grid level 2 the efficiency over the whole grid increases about 50 % at the massflow rate of 20 %. At the design point the increment was only 20 %. At the massflow rate of 160 % of the design point value the efficiency was negative at the grid level 3. This means that the pump does not increase the mechanical energy although the static pressure rises. The static pressure rise is obtained from the kinetic energy. At the grid level 2 the efficiency becomes positive and so predicting increasing mechanical energy flux over the pump.

7 Discussion

The $k-\epsilon$ turbulence model with a rotation correction works well in this case, whereas the SSG model had problems in convergence. The SSG calculation on the second densiest grid level failed many times despite low Courant numbers (0.5). The multigrid acceleration was also left out in the SSG calculation, but the result was the same, the calculation did not converge. On the third grid level the calculation converged and the resuls were realistic. The efficiency given by SSG model was better than that of $k-\epsilon$-model and it was also closer to the value read from the manufacturer's data sheet. Because that result is obtained from the third grid level, we cannot make any conclusion on the accuracy of the Reynolds stress model in this case. But we can say that, it is not robust enough for the industrial applications. It requires also about 1.7 times the memory used by the $k-\epsilon$ model. That is also one constraining property of the Reynold stress models considering the industrial use.

There were quite considerable differences when comparing the results from different grid levels. The grid level 3 is defenitely too coarse and the run at the first grid level takes too much time for practical purposes. So the most usable grid level in the engineering problems is level 2. That level predicts the most features in the flow field and the overall results are reasonable. If the user is interested in small flow details, then the simulation should be run also at the finest grid level. However, as far as the efficiency and head are concerned, the first level is required. With a low-Reynolds number model the number of grid points is, as a consequence, quite large.

One of the main problems in the evaluation of a flow solver in complex cases is the lack of measured data. Also in this case only the smoothed head and power curves were available. In order to obtain good verification of calculated results much more detailed measurements should be available. For example, velocity profiles and pressure distributions could be very helpful. Because of smoothing the errors in the reference values can be the same order of magnitude as the difference between the calculated value and the value obtained from the manufacturer's curves.

References

[1] *FINFLO User Manual version 2.2*, 1997.

[2] K.-Y. Chien. Predictions of Channel and Boundary-Layer Flows with a Low-Reynolds-Number Turbulence Model. *AIAA Journal*, Vol. 20, No. 1, pp. 33–38, Jan 1982.

[3] C.G. Speziale, S. Sarkar, and T.B. Gatski. Modelling the pressure-strain correlation of turbulence: and invariant dynamical systems approach. *Journal of Fluid Mechanics*, Vol. 227, pp. 245–272, 1991.

[4] T. Siikonen. An Application of Roe's Flux-Difference Splitting for the $k-\epsilon$ Turbulence Model. *International Journal for Numerical Methods in Fluids*, Vol. 21, pp. 1017–1039, 1995.

[5] *IGG, Interactive Geometry Modeller and Grid Generator User Manual, Version 3.4-6.* 5, avenue Franklin Roosevelt, 1050 Brussels, Belgium, 1996.

[6] Juha Ojala. Pyörimisliikekorjaus $k-\epsilon$-turbulenssimalliin. Technical report, Sovelletun termodynamiikan laboratorio, TKK, Heinäkuu 1997.

[7] S. V. Patankar J. H. G. Howard and R. M. Bordynuik. Flow Prediction in Rotating Ducts Using Coriolis-Modified Turbulence Models. *Journal of Fluids Engineering*, Vol. 102, December 1980.

[8] Andrei Khodak and Charles Hirsch. Second-Order Non-Linear k-ϵ Models with Explicit Effect of Curvature and Rotation. In *the Third ECCOMAS Computational Fluid Dynamics Conference*, Paris, France, 9-13 September 1996.

[9] P.P. Rautaheimo and T. Siikonen. Implementation of the Reynolds-stress Turbulence Model. In *Proceedings of the ECCOMAS Congress*, Paris, Sept. 1996.

[10] N. Shima. A Reynolds-Stress Model for Near-Wall and Low-Reynolds-Number Regions. *Journal of Fluids Engineering*, Vol. 110, pp. 38–44, 1988.

[11] H.-C. Chen. Assessment of a Reynolds Stress Closure Model for Appendage-Hull Junction Flows. *Journal of Fluids Engineering*, Vol. 117, No. 5, pp. 557–563, Dec 1995.

Appendix A Streamlines in the Impeller

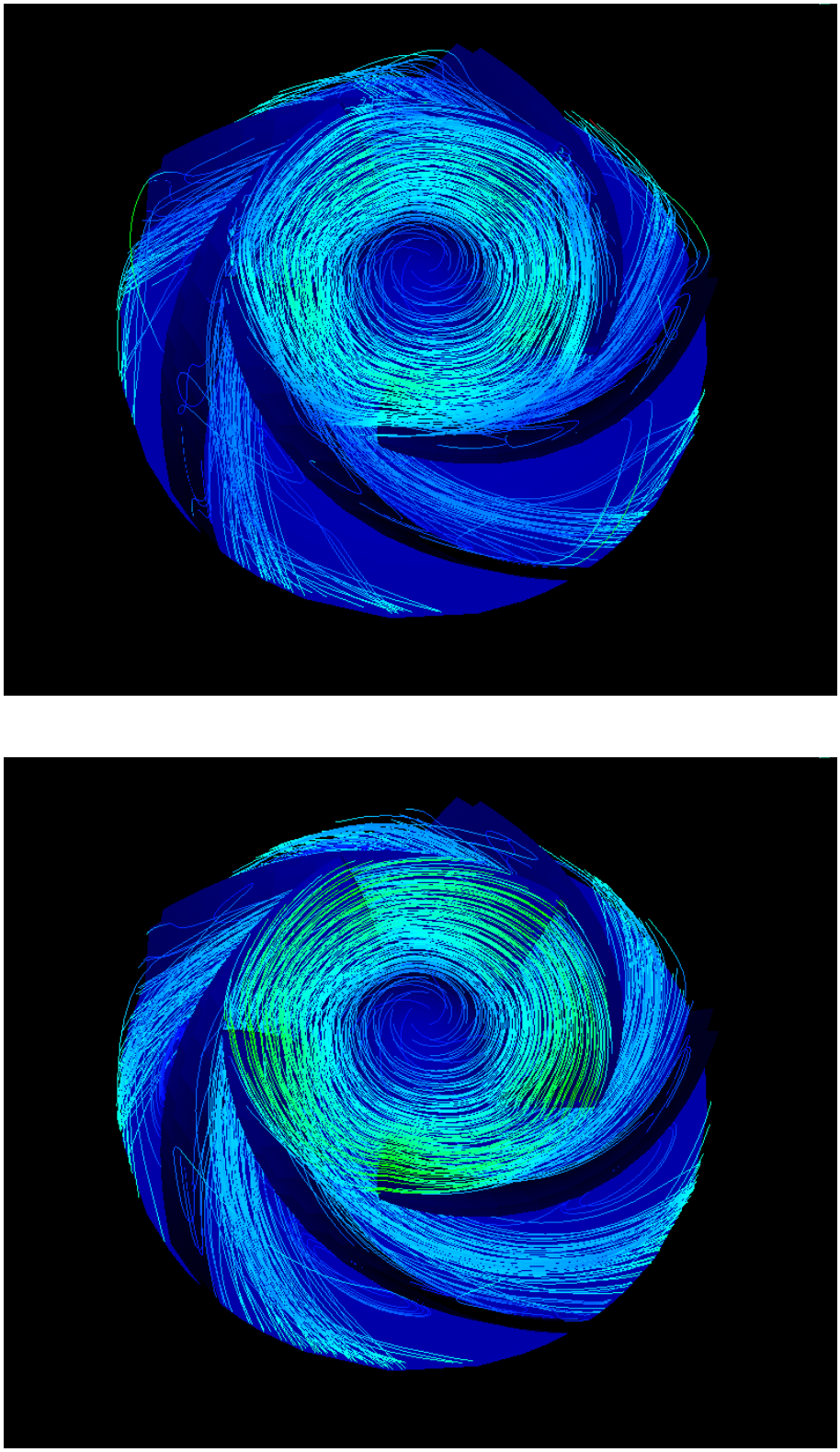

Fig. 7: Streamlines in the impeller (massflows 20 % and 40 %).

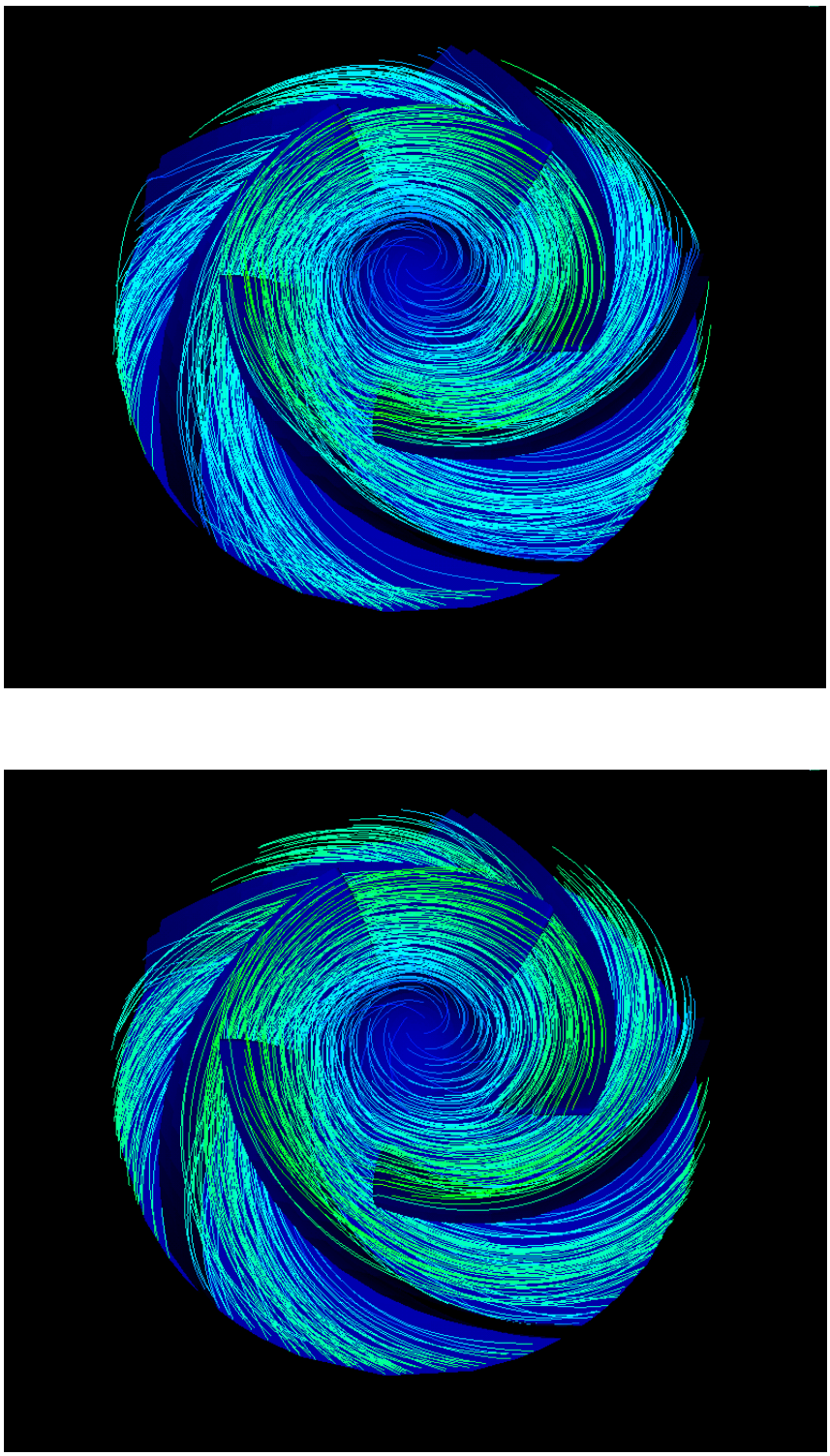

Fig. 8: Streamlines in the impeller (massflows 60 % and 80 %).

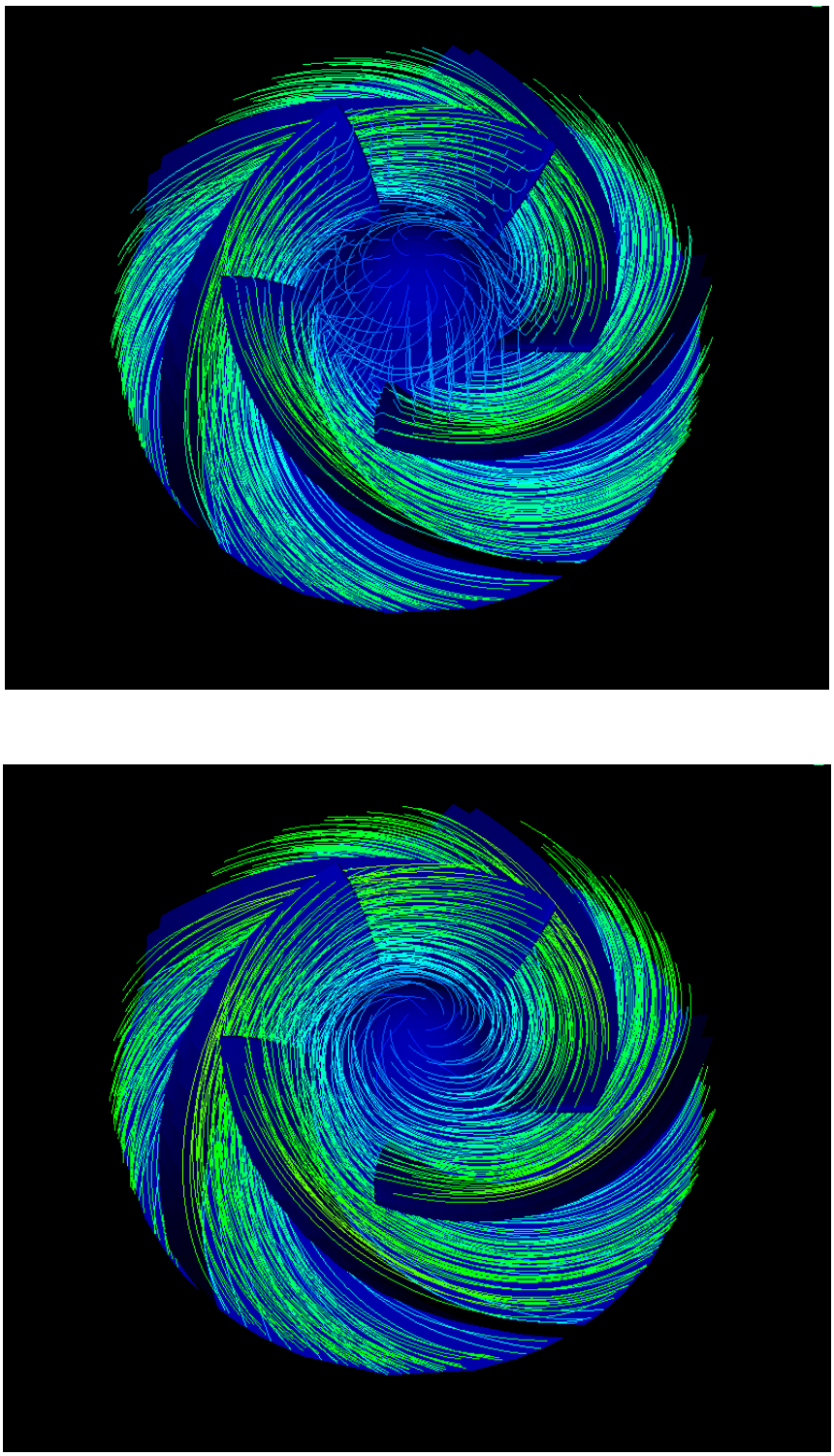

Fig. 9: Streamlines in the impeller (massflows 100 % and 120 %).

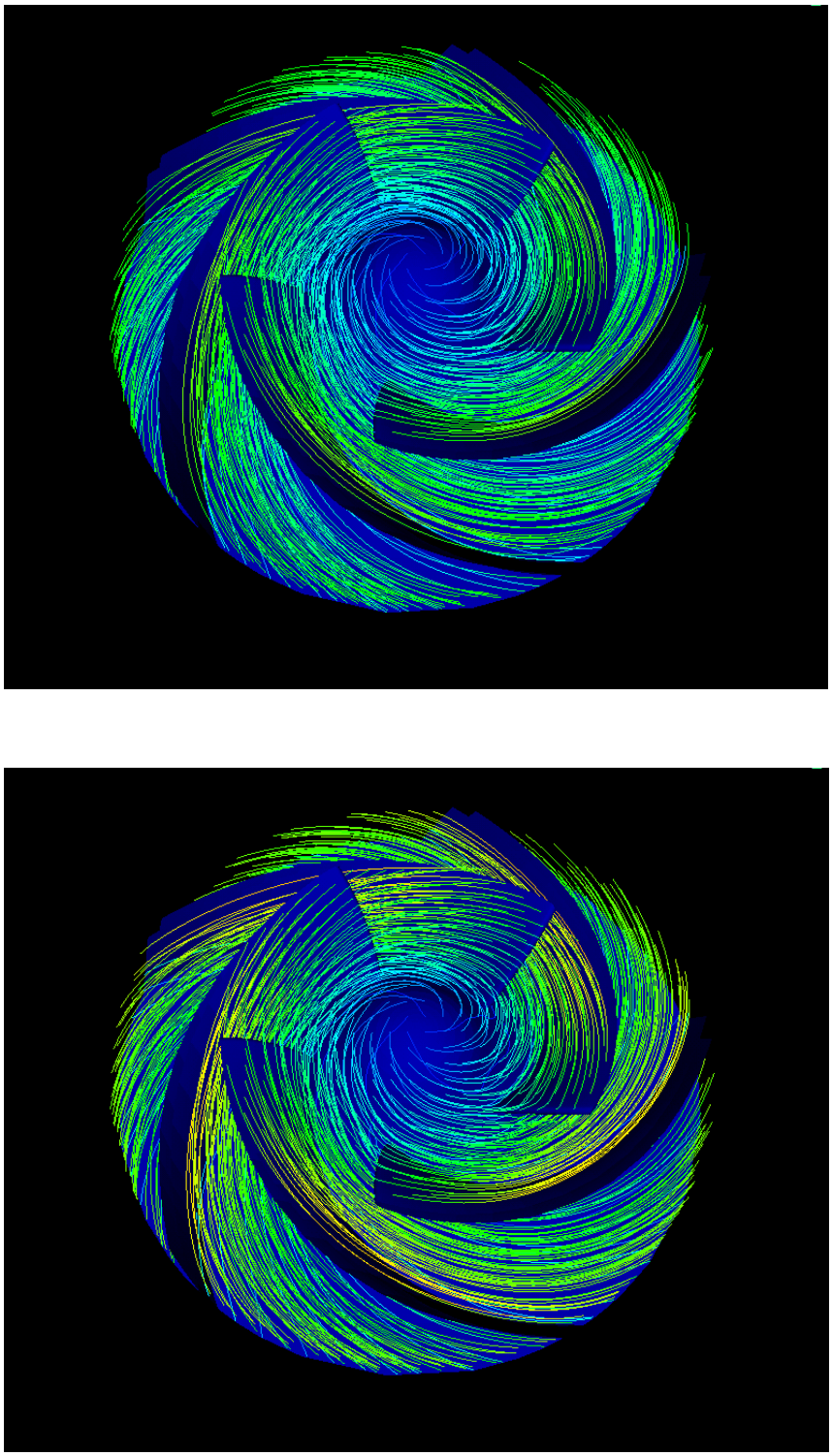

Fig. 10: Streamlines in the impeller (massflows 140 % and 160 %).

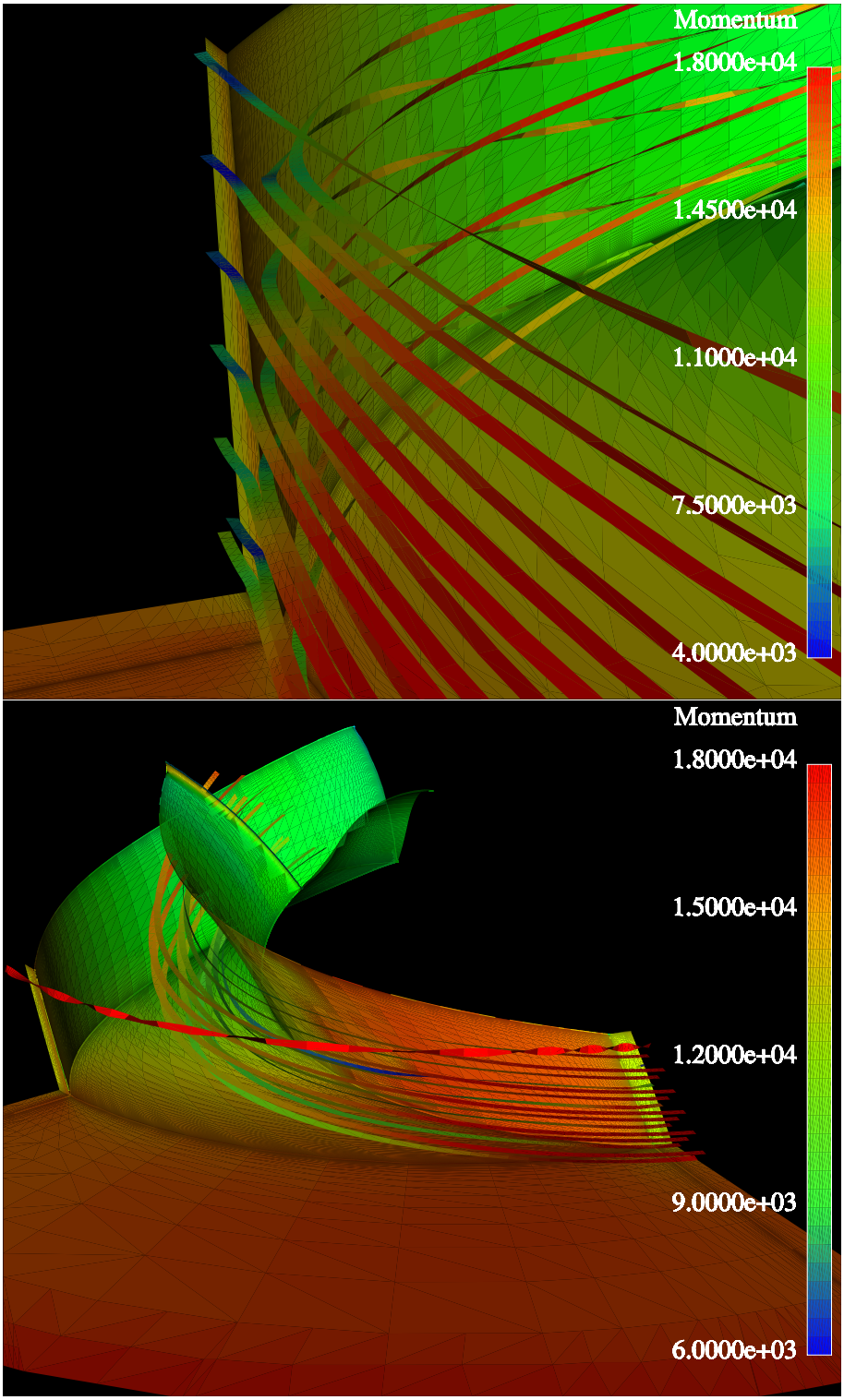

Fig. 11: Streamlines near the suction and pressure side (level 1, massflow 100 %).

Appendix B Velocity Vectors in the Center of the Cascade

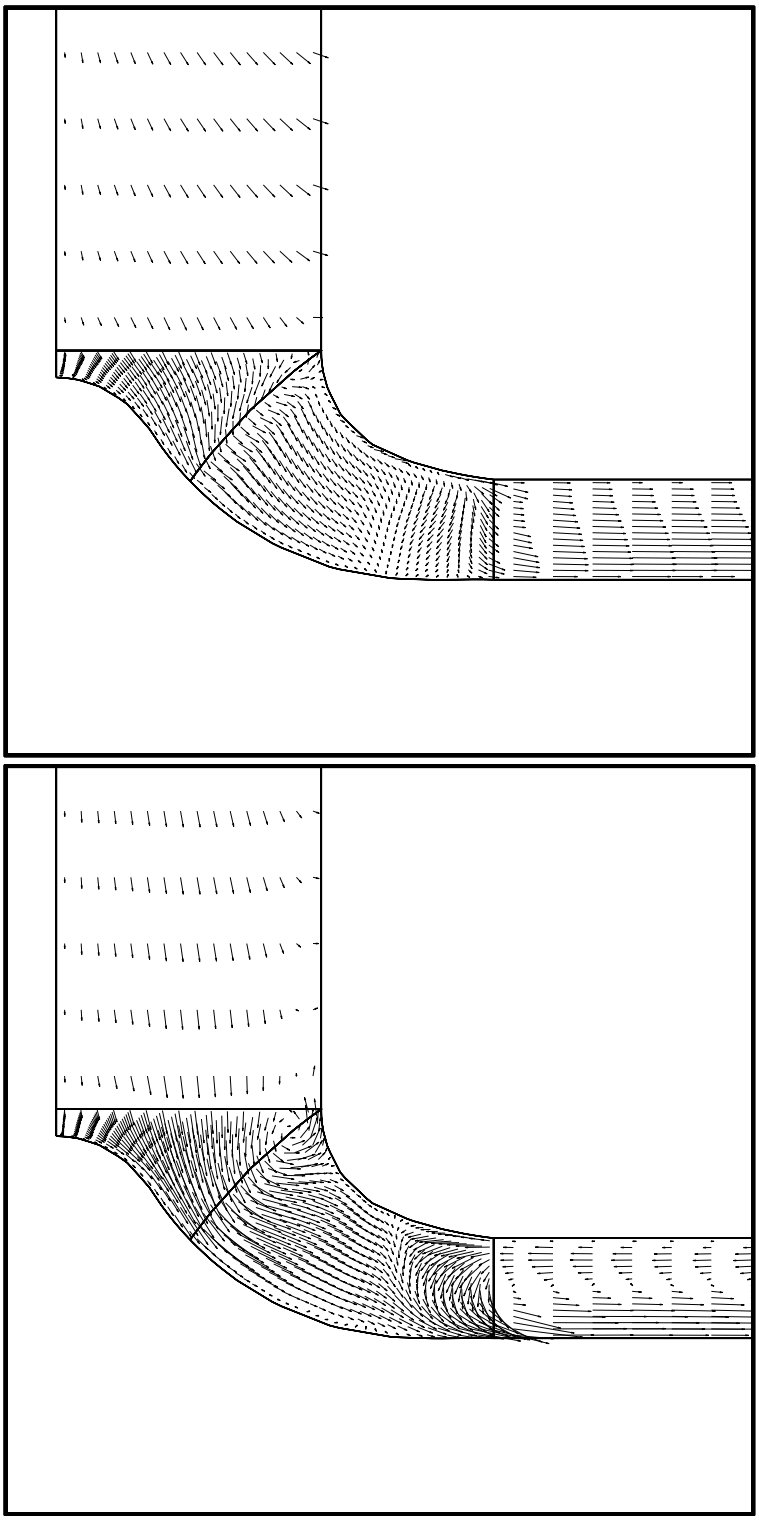

Fig. 12: $Q/Q_0 = 20\%$, level 3 and level 2

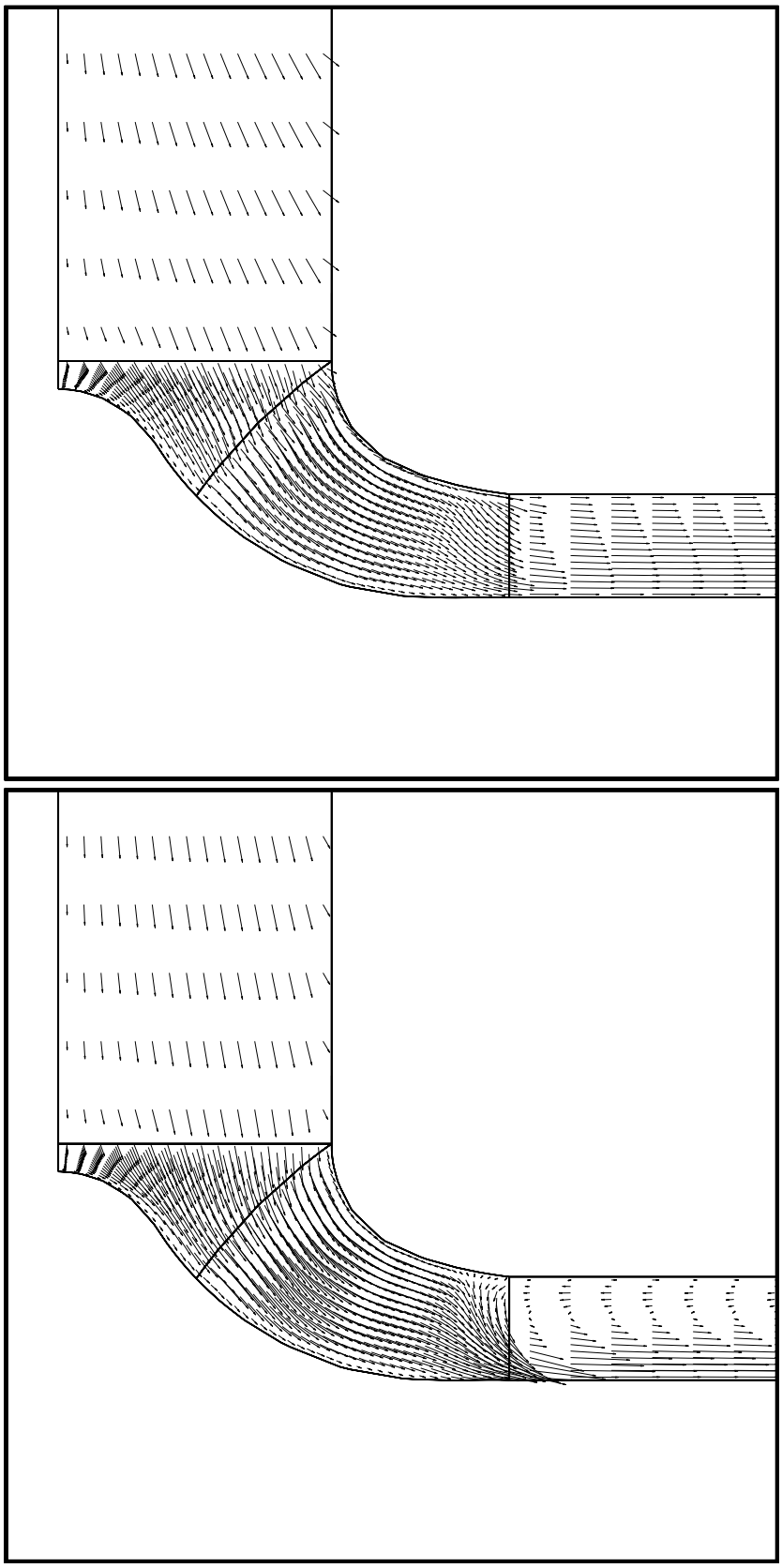

Fig. 13: $Q/Q_0 = 40\%$, level 3 and level 2.

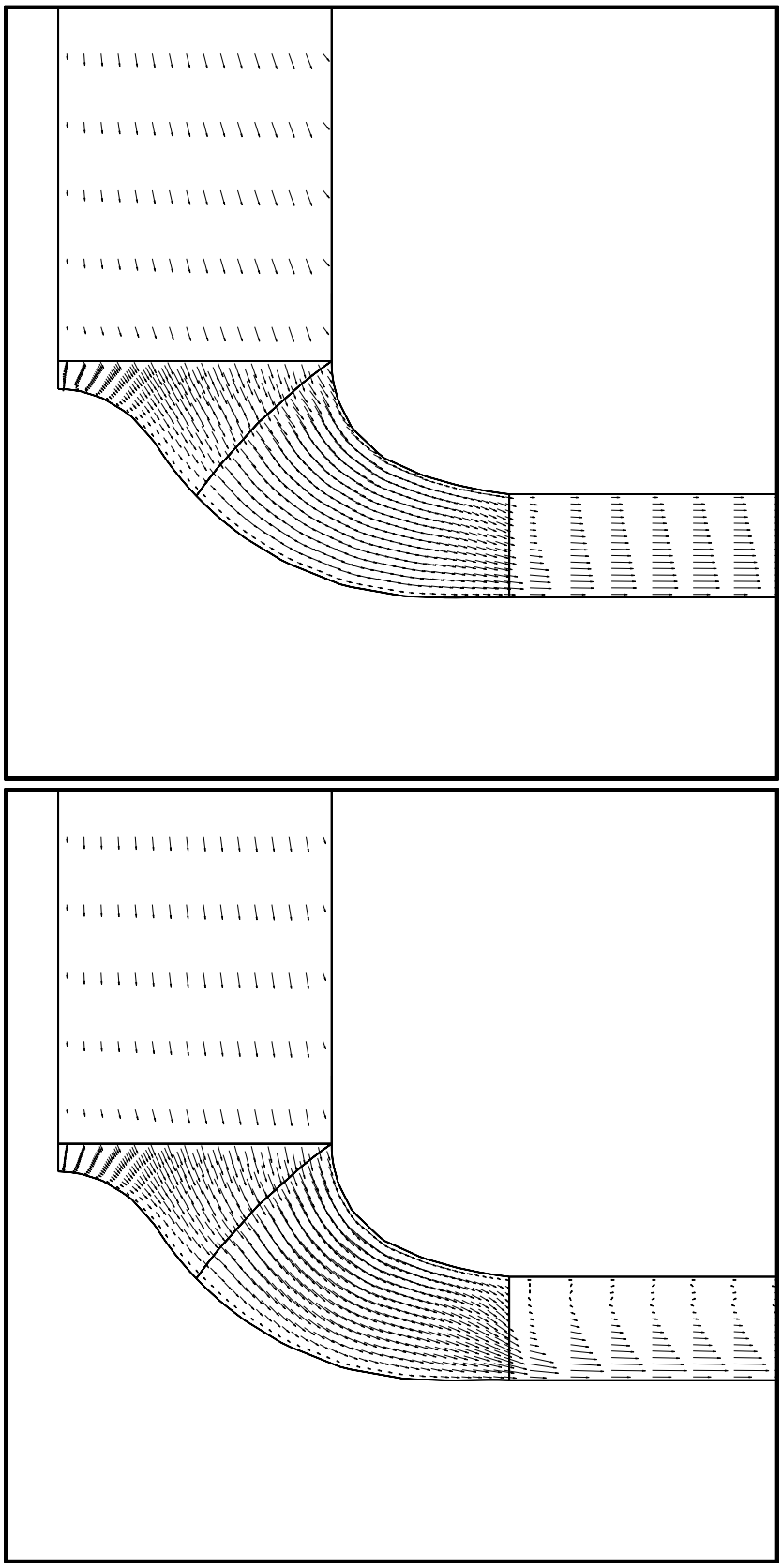

Fig. 14: $Q/Q_0 = 60\%$, level 3 and level 2.

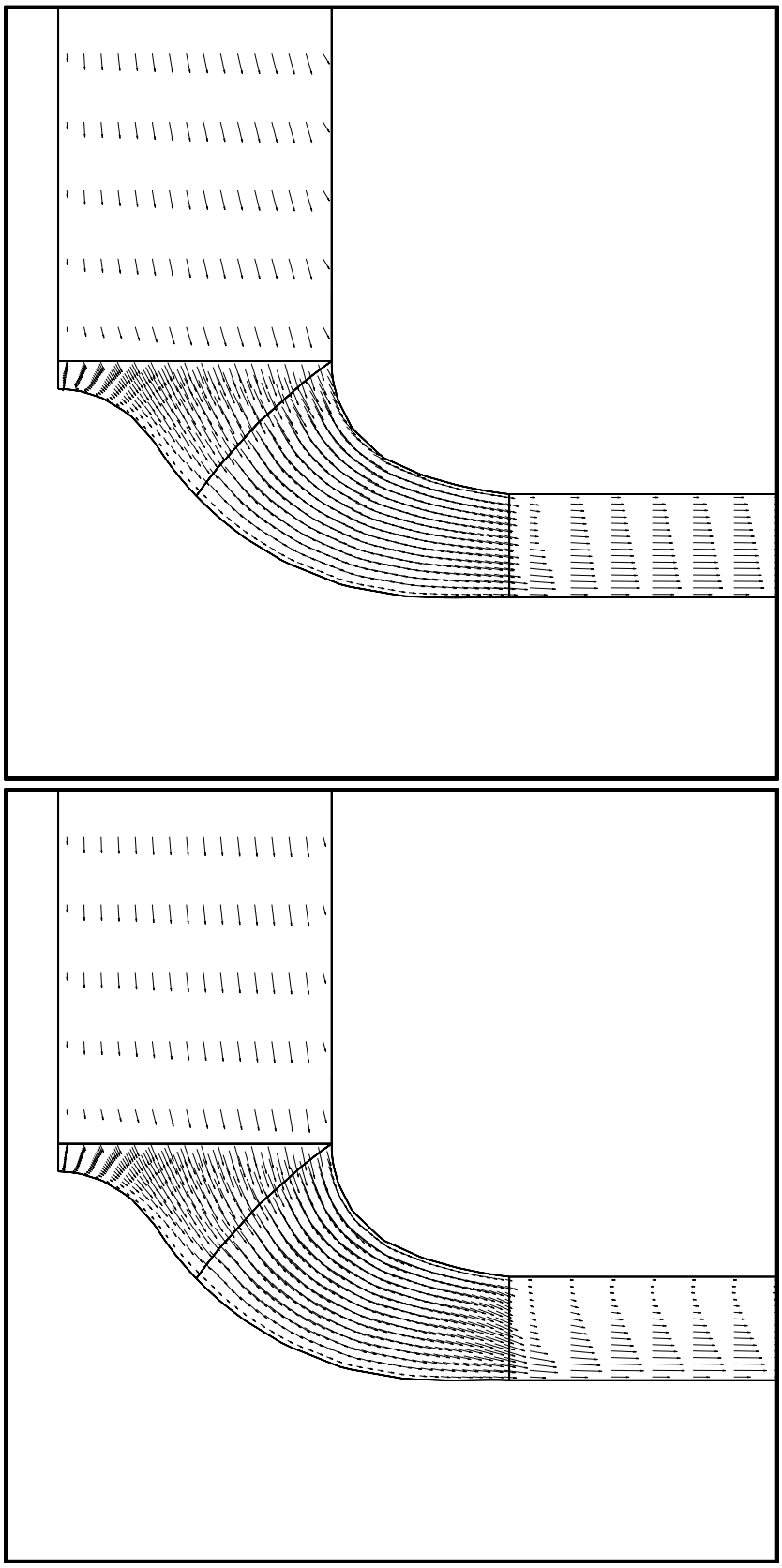

Fig. 15: $Q/Q_0 = 80\%$, level 3 and level 2.

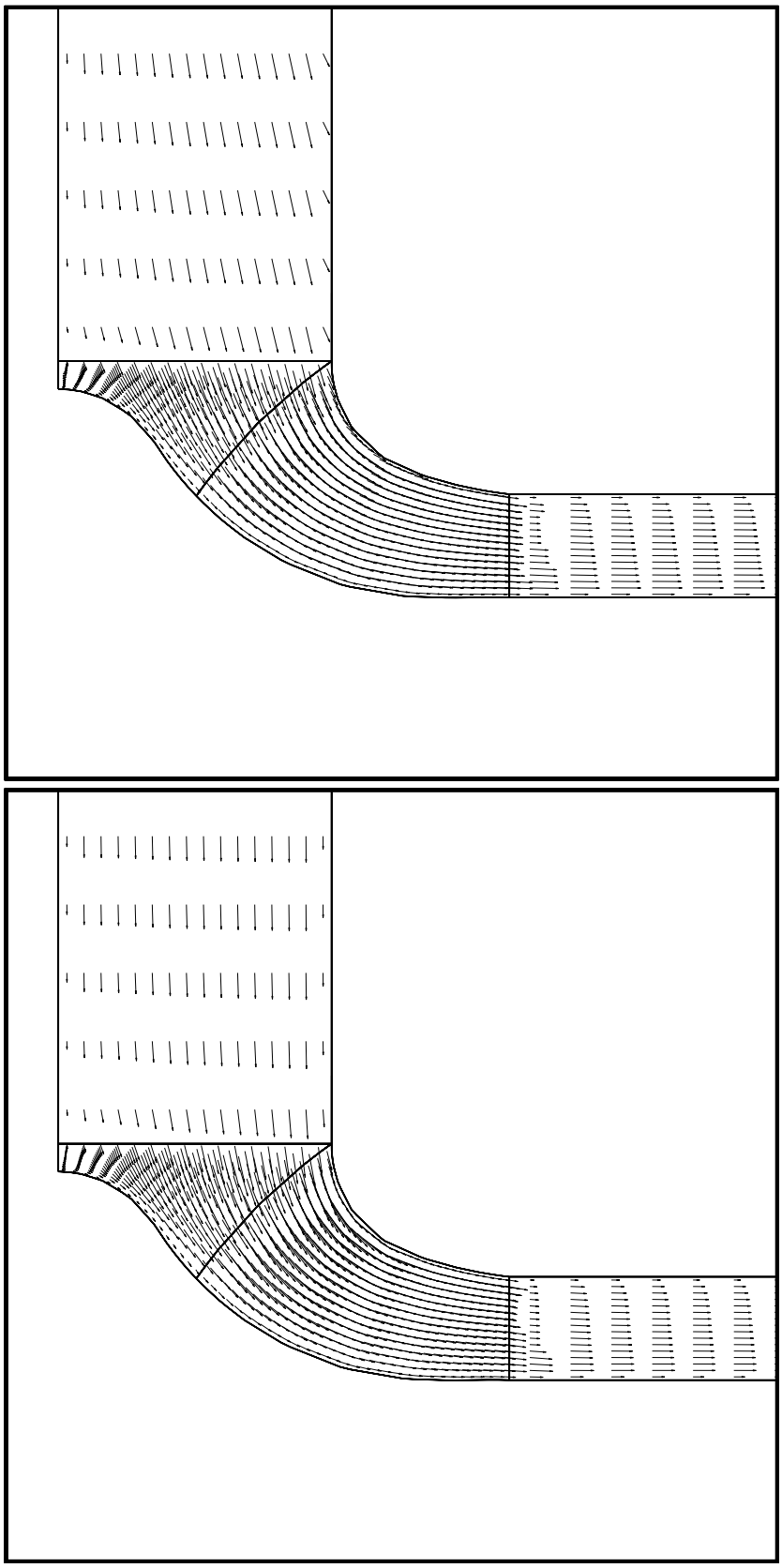

Fig. 16: $Q/Q_0 = 100\%$, level 3 and level 2.

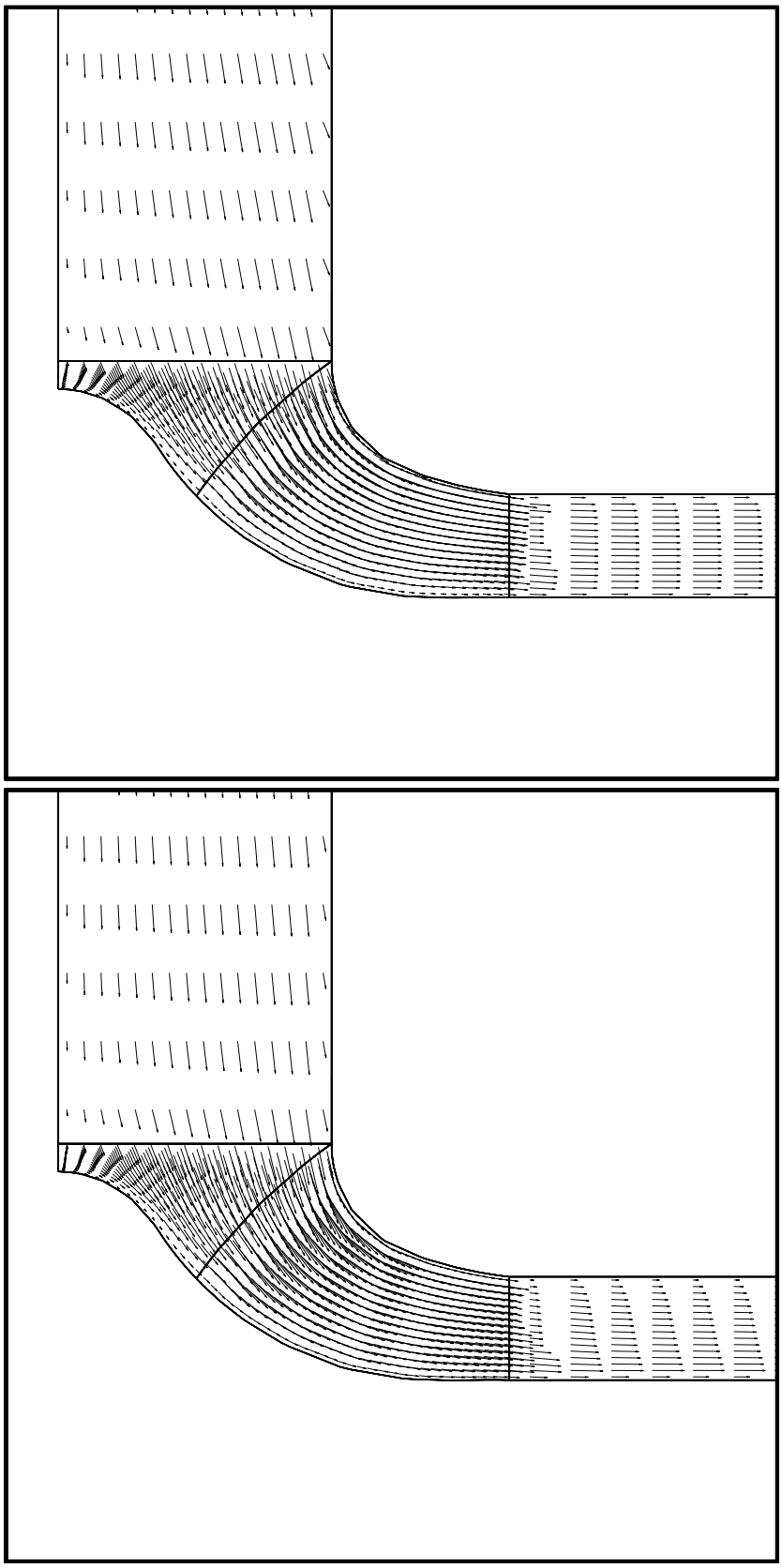

Fig. 17: $Q/Q_0 = 120\%$, level 3 and level 2.

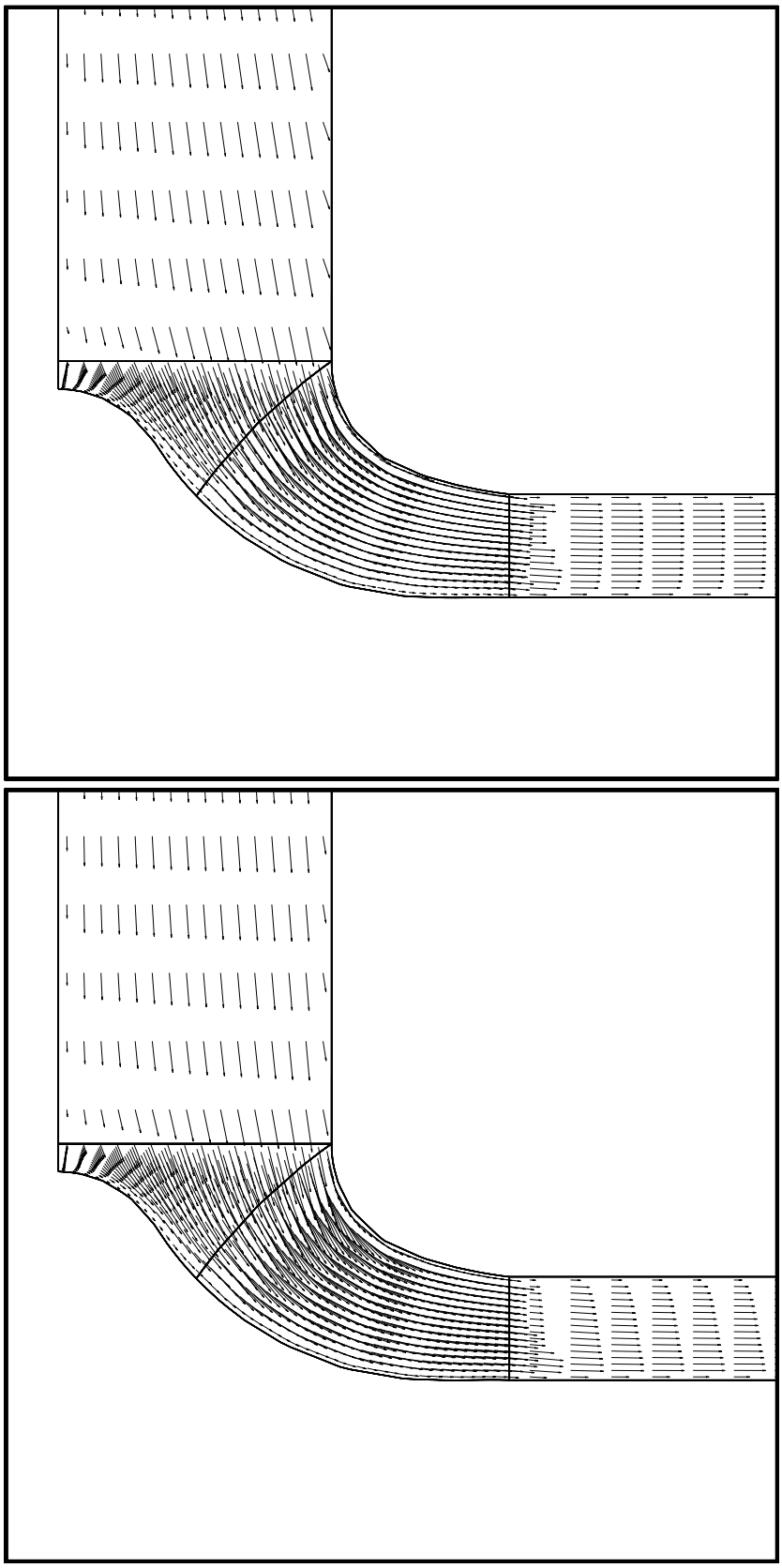

Fig. 18: $Q/Q_0 = 140\%$, level 3 and level 2.

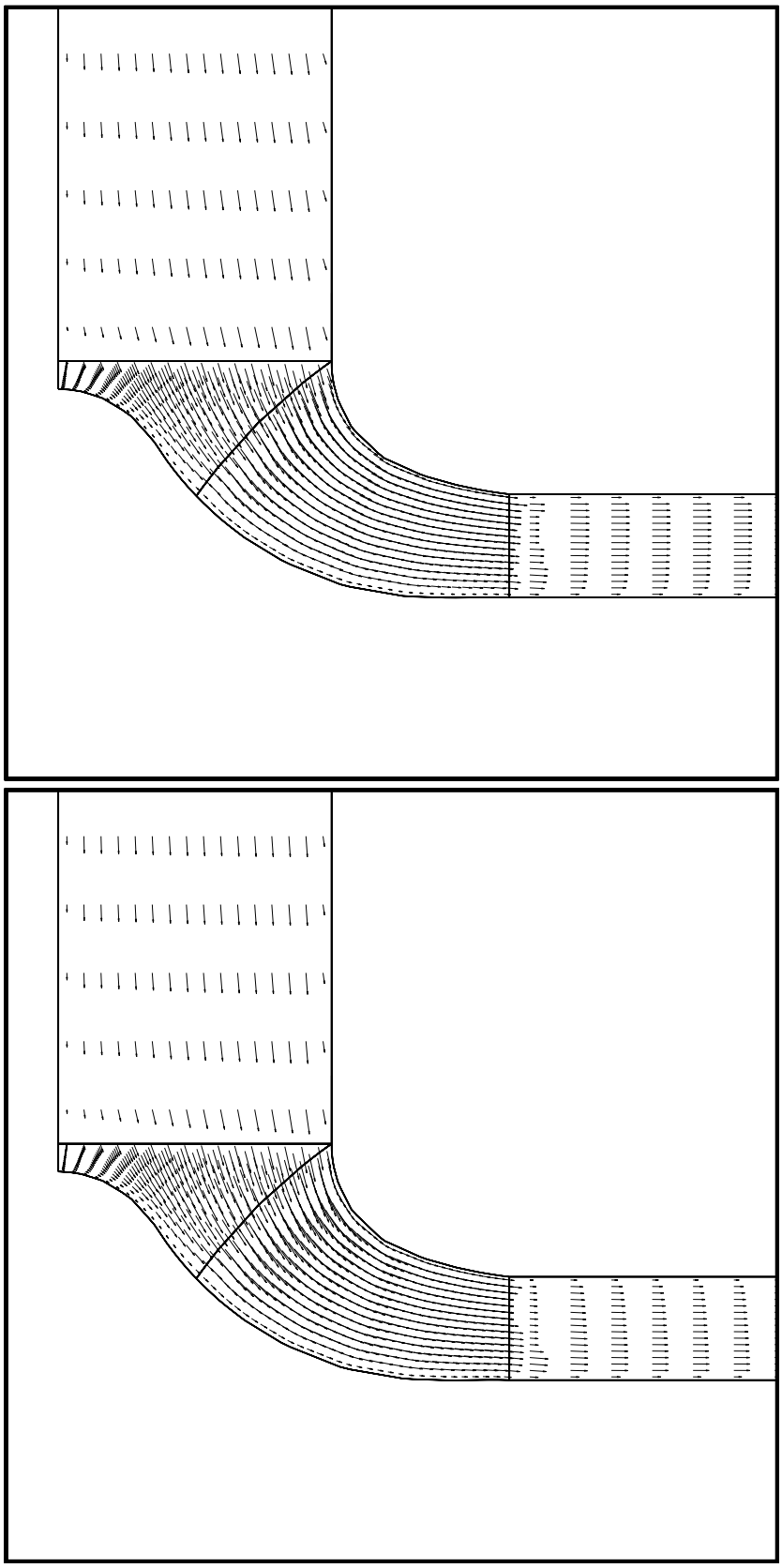

Fig. 19: $Q/Q_0 = 160\%$, level 3 and level 2.

Appendix C Velocity Vectors on the Pressure and Suction Side

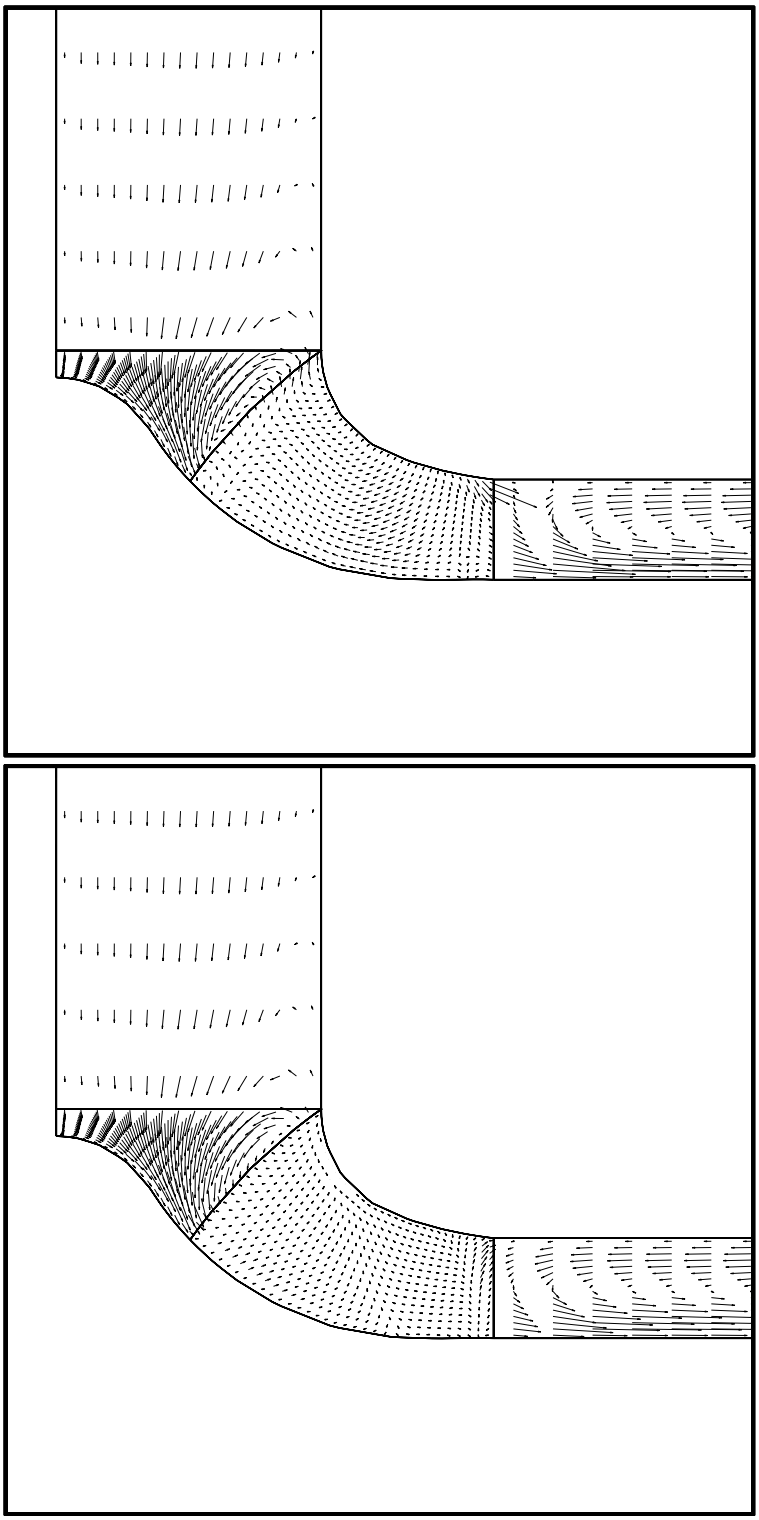

Fig. 20: The pressure and suction side, $Q/Q_0 = 20\%$, level 2.

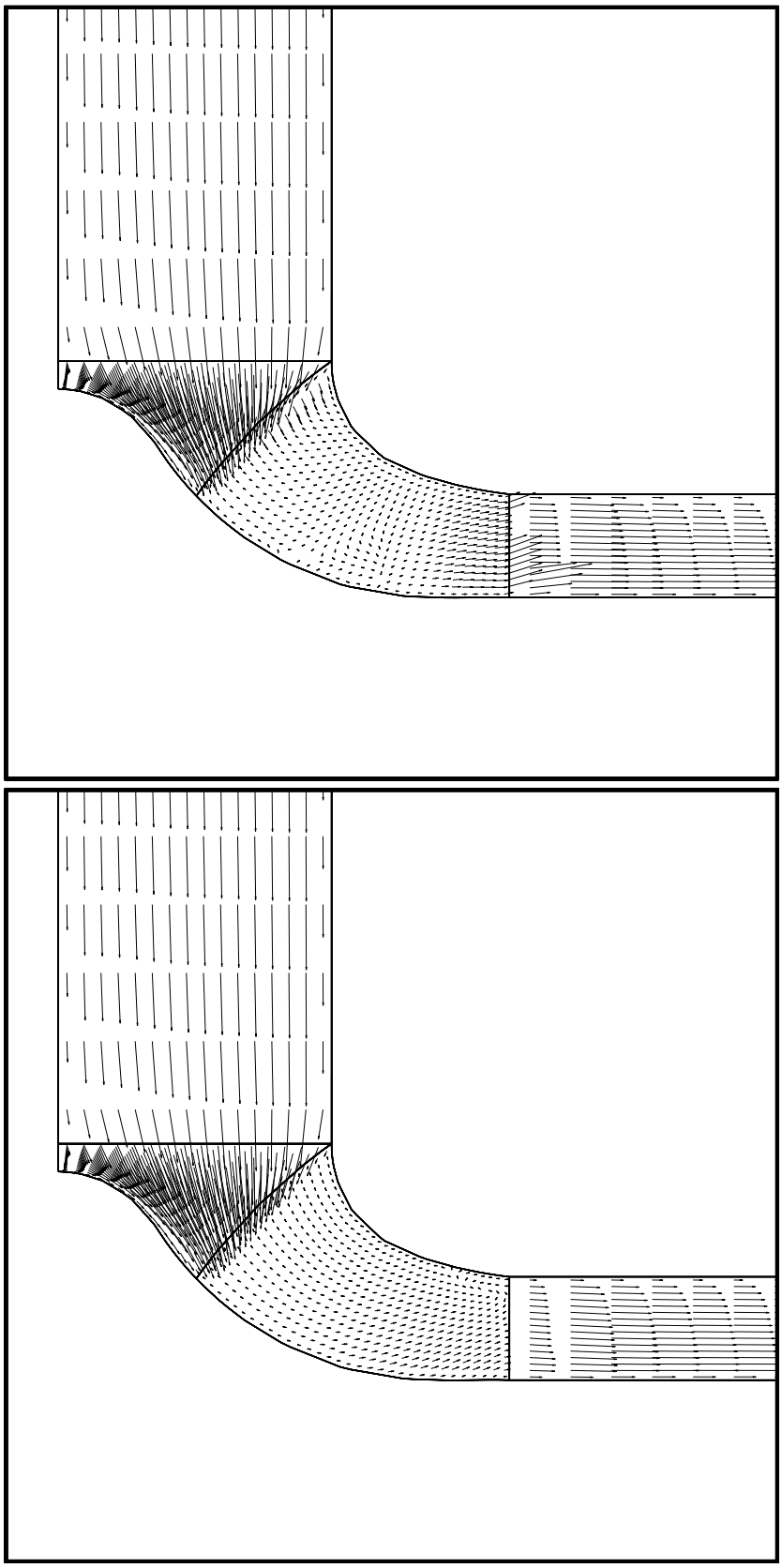

Fig. 21: The pressure and suction side, $Q/Q_0 = 100\%$, level 2.

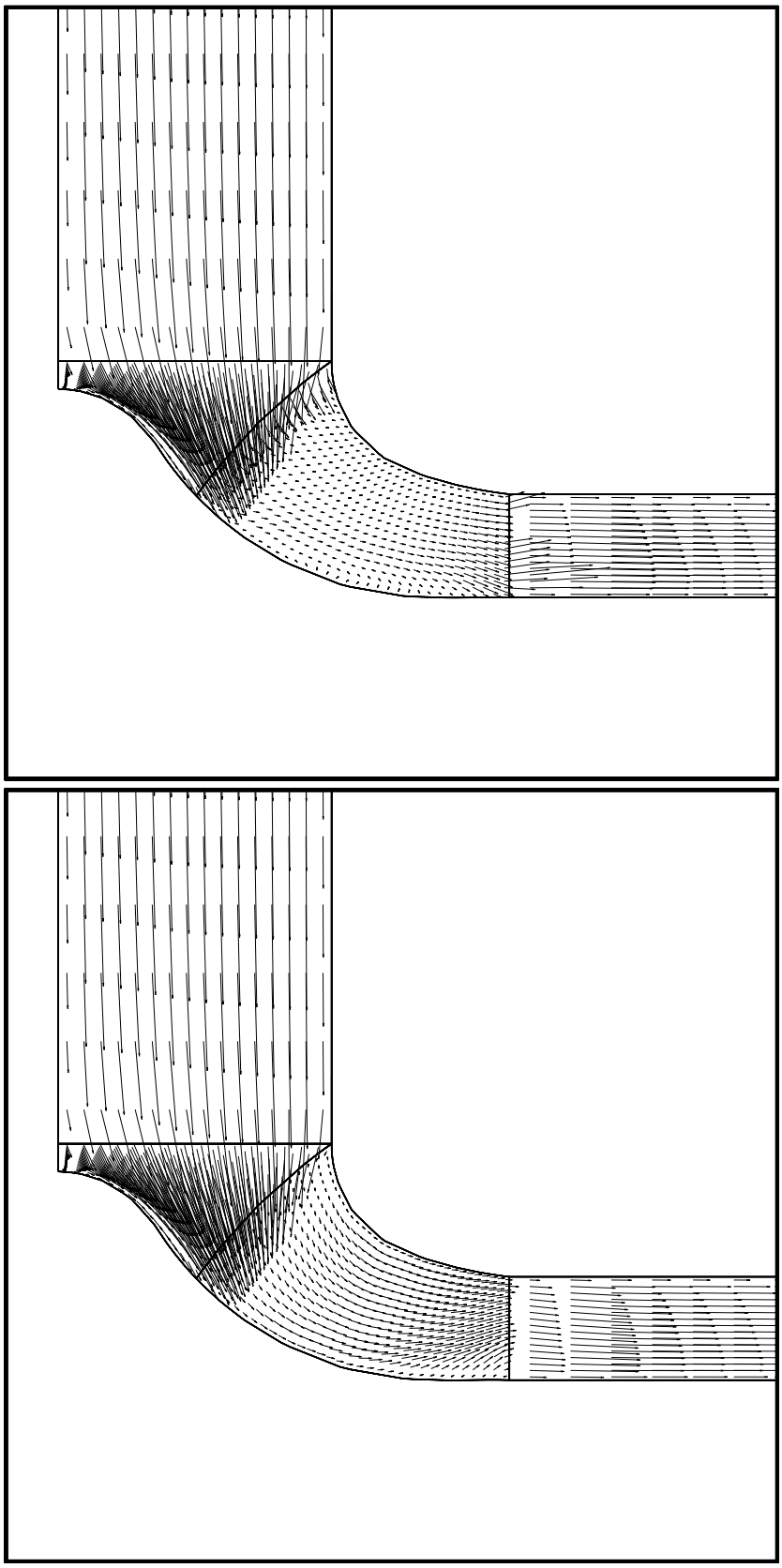

Fig. 22: The pressure and suction side, $Q/Q_0 = 160\%$, level 2.

Appendix D Static Pressure on the Impeller Surface

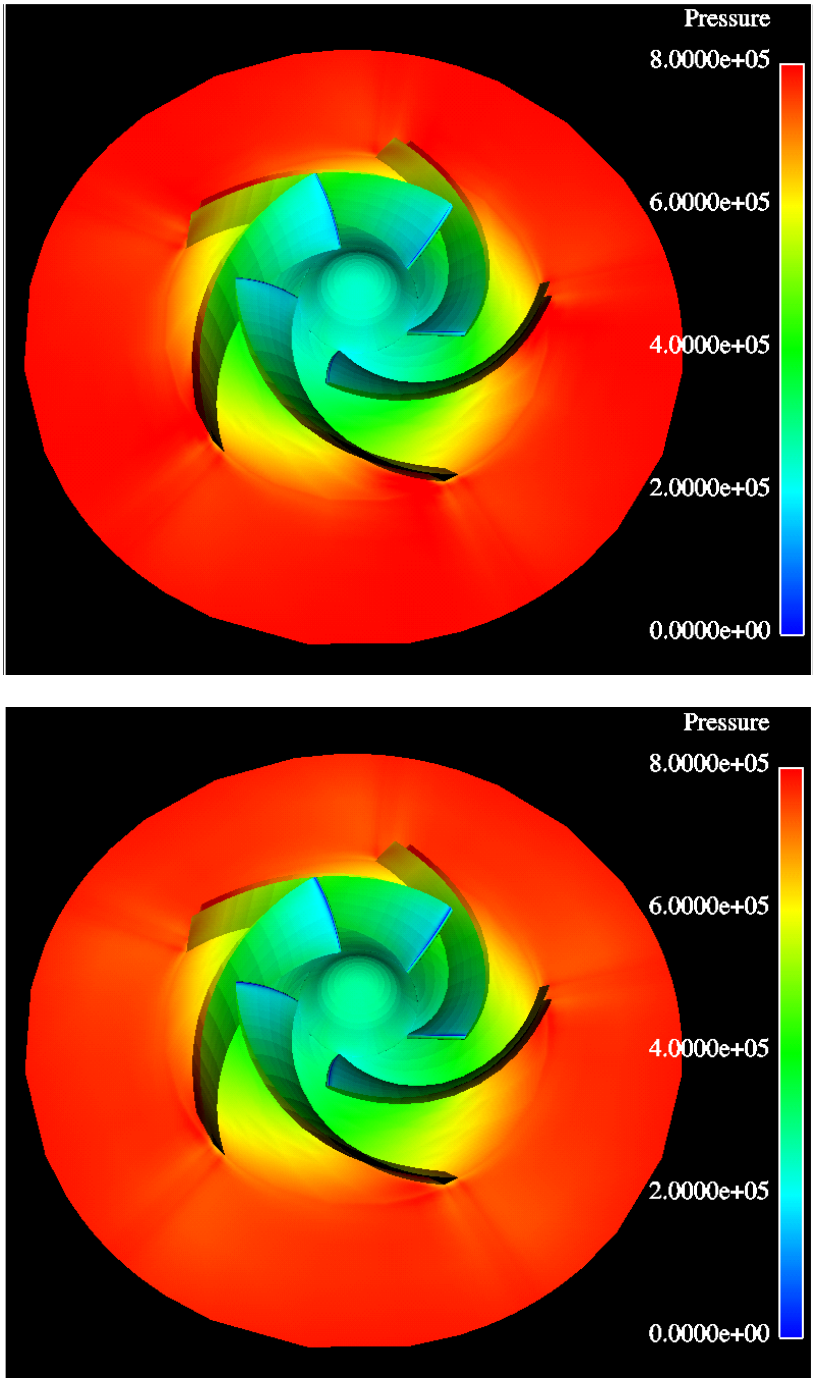

Fig. 23: Static pressure on the impeller surface (massflows 20 % and 40 %, level 2)

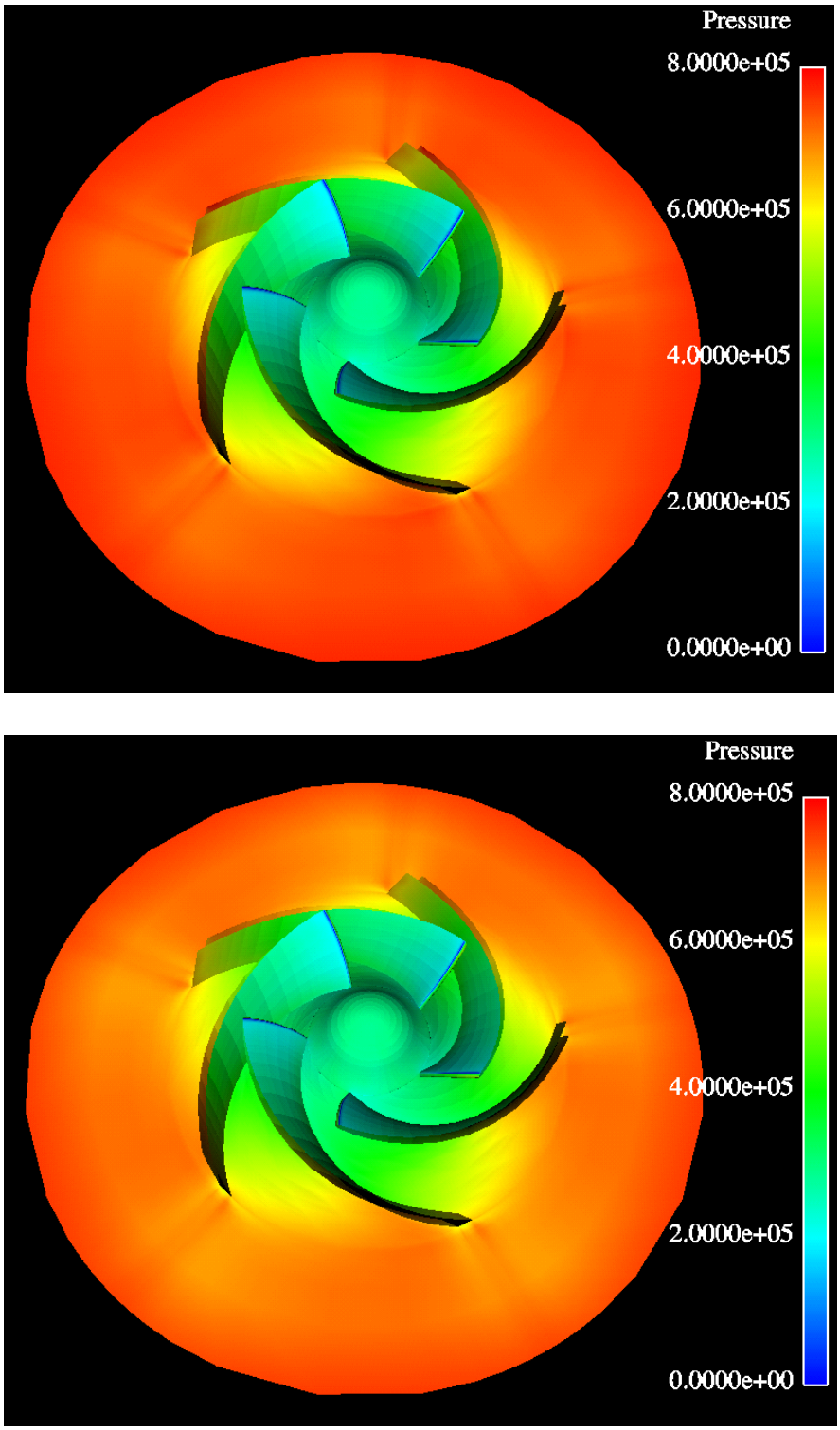

Fig. 24: Static pressure on the impeller surface (massflows 60 % and 80 %, level 2)

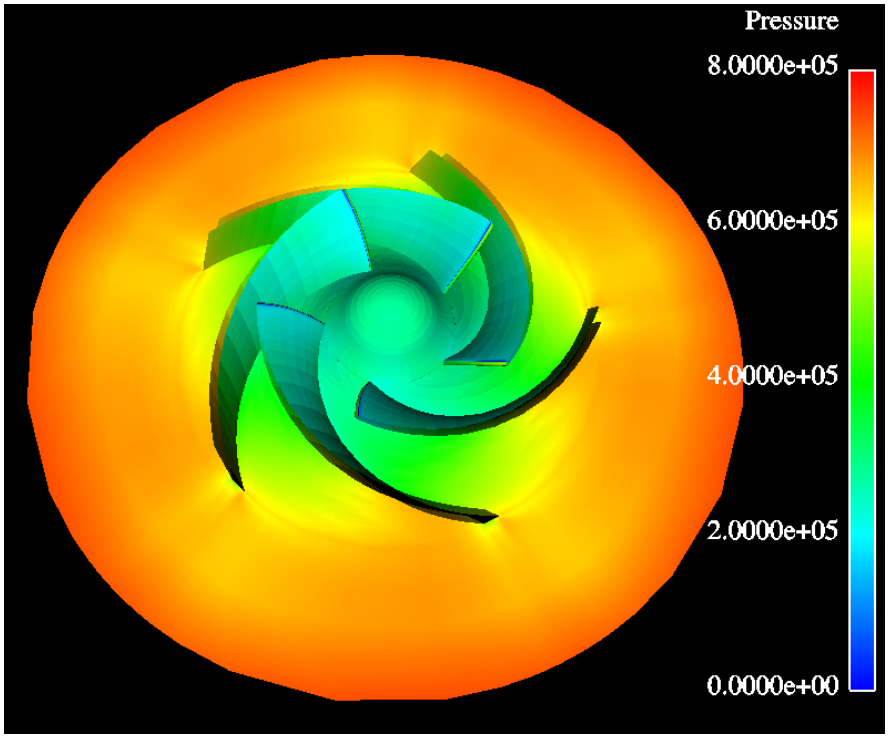

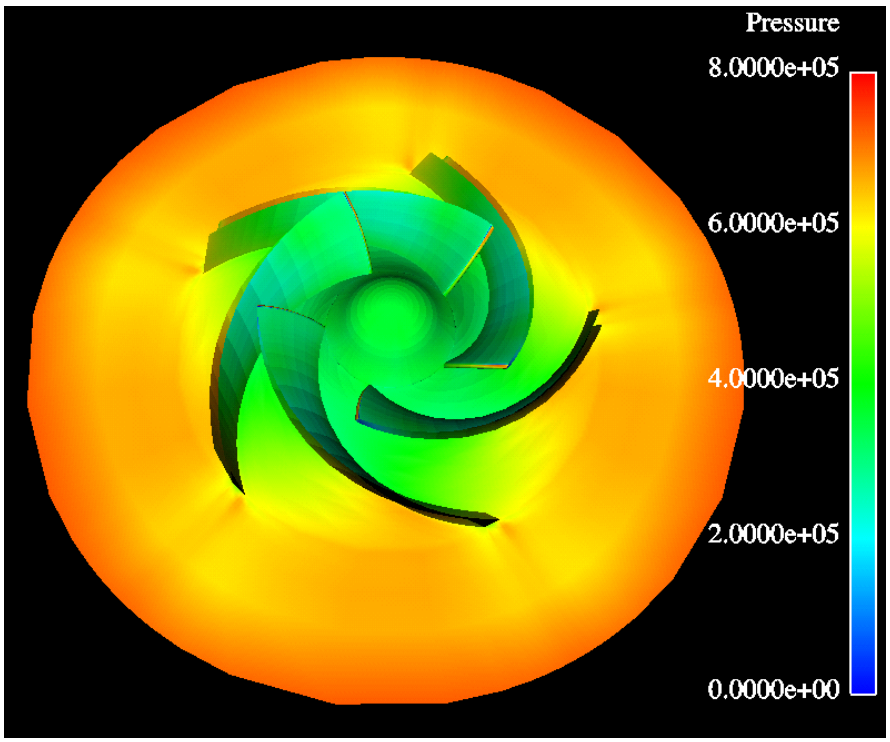

Fig. 25: Static pressure on the impeller surface (massflows 100 % and 120 %, level 2)

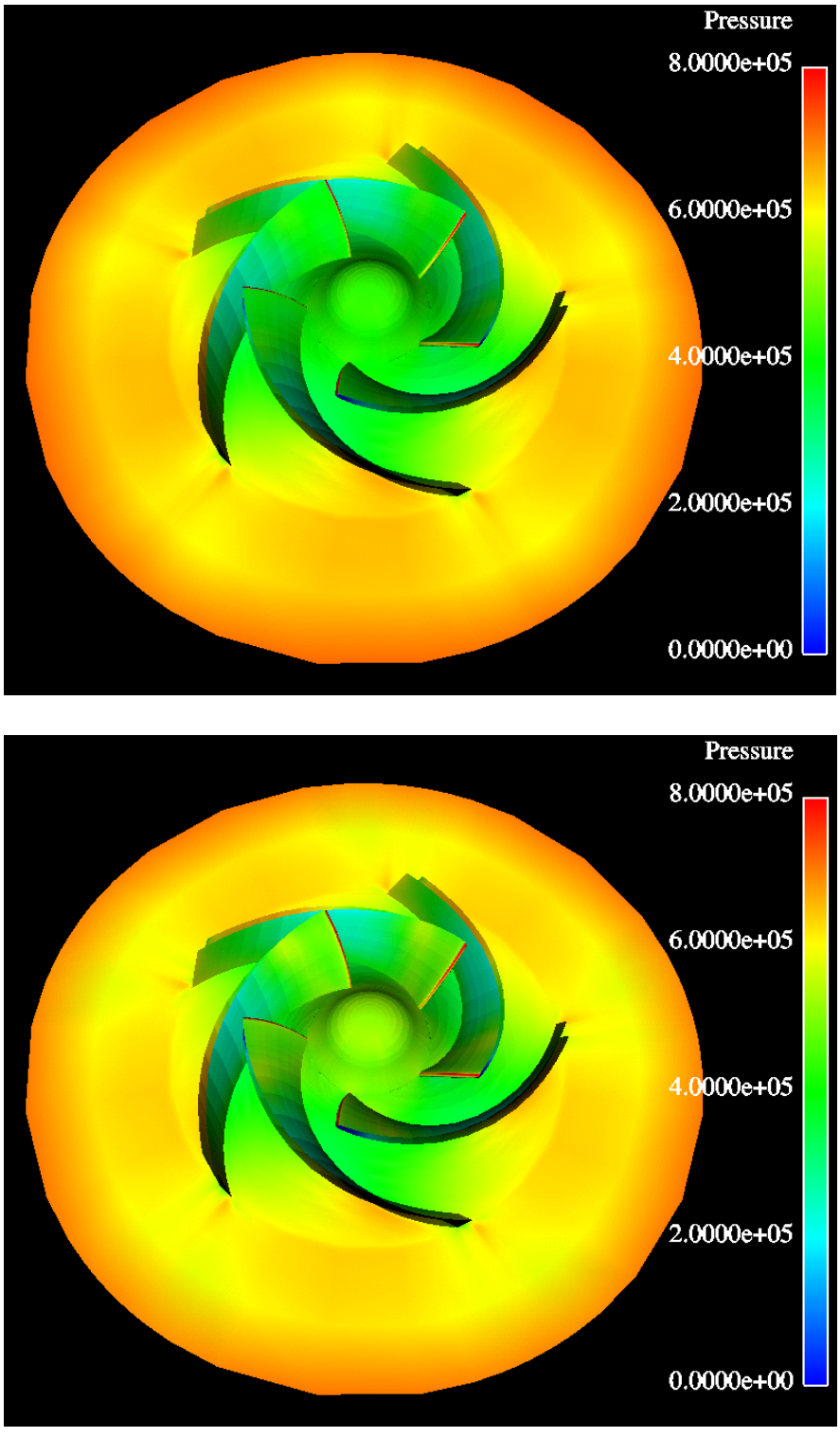

Fig. 26: Static pressure on the impeller surface (massflows 140 % and 160 %, level 2)

Appendix E Total Pressure on the Pressure and on the Suction Surfaces

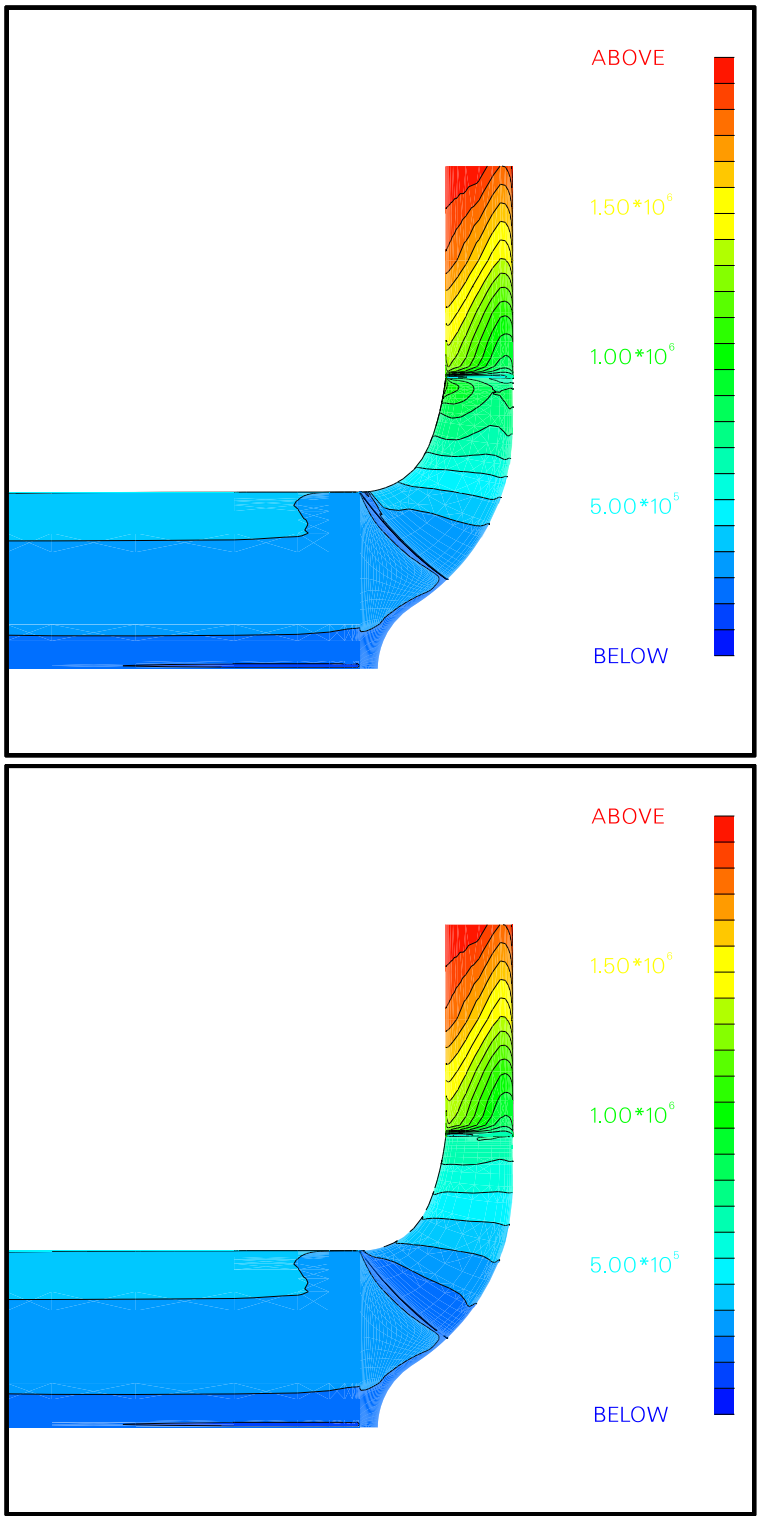

Fig. 27: Total pressure on the pressure and on the suction side (massflow 20 %, level 2)

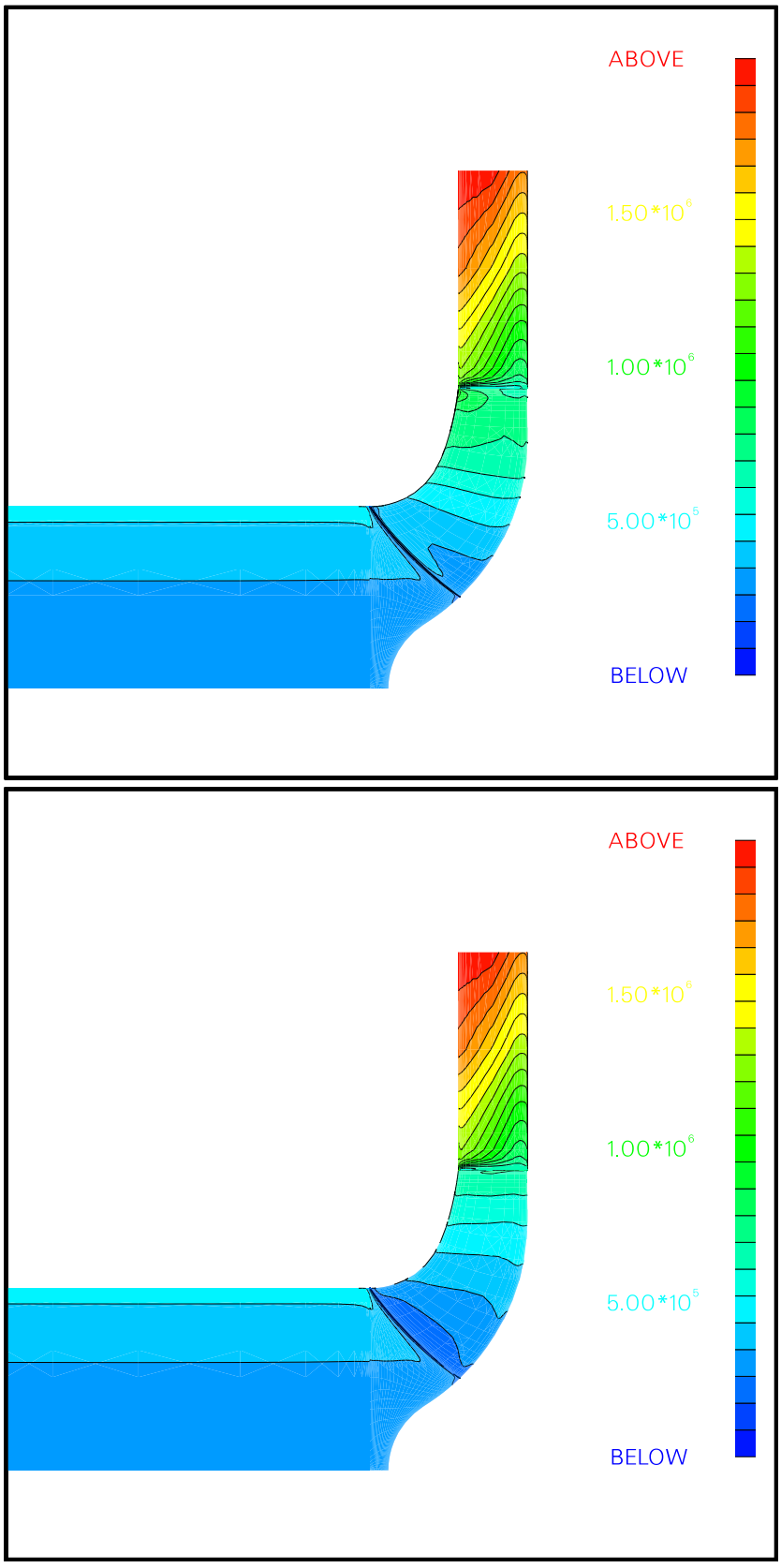

Fig. 28: Total pressure on the pressure and on the suction side (massflow 40 %, level 2)

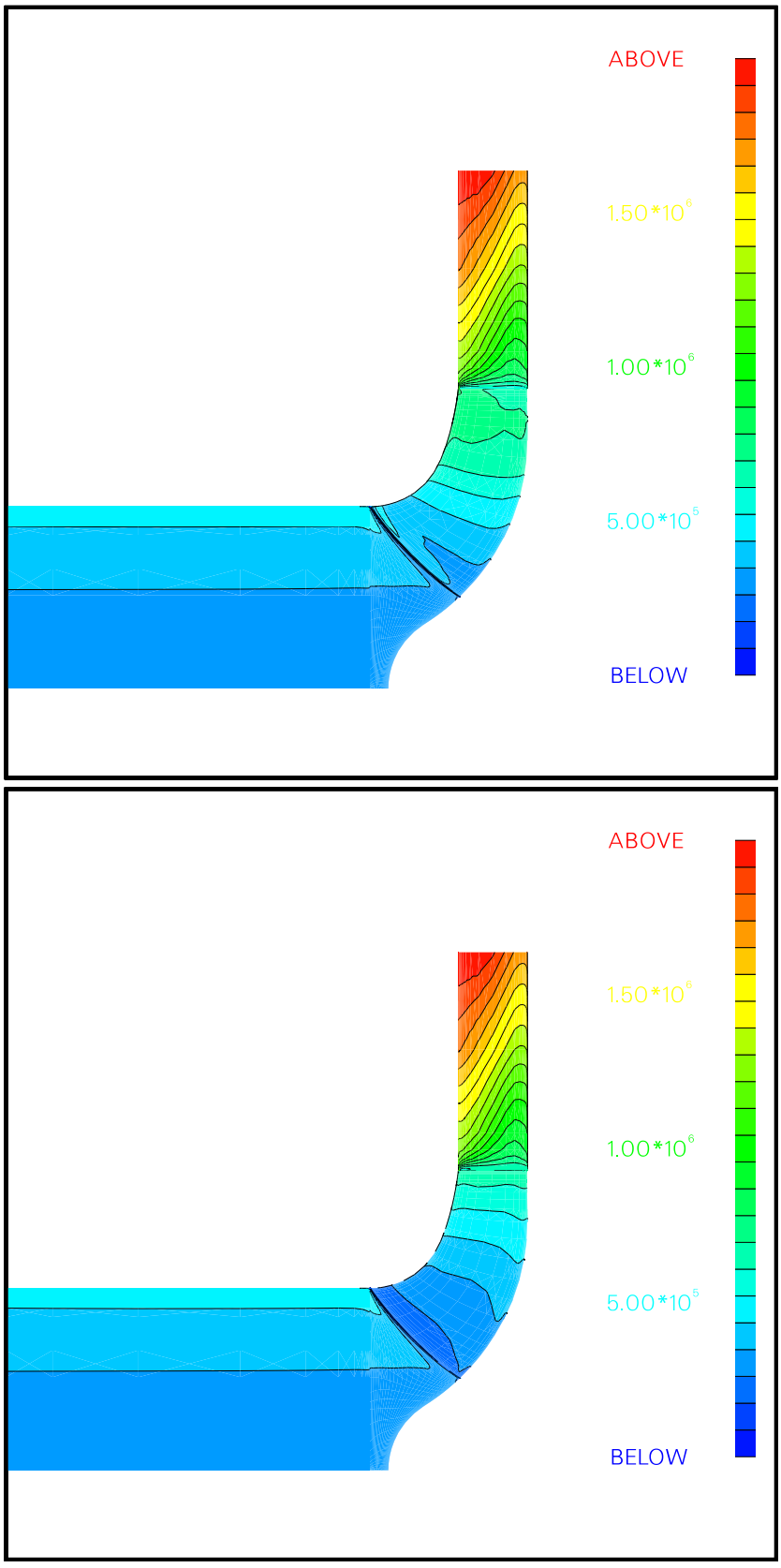

Fig. 29: Total pressure on the pressure and on the suction side (massflow 60 %, level 2)

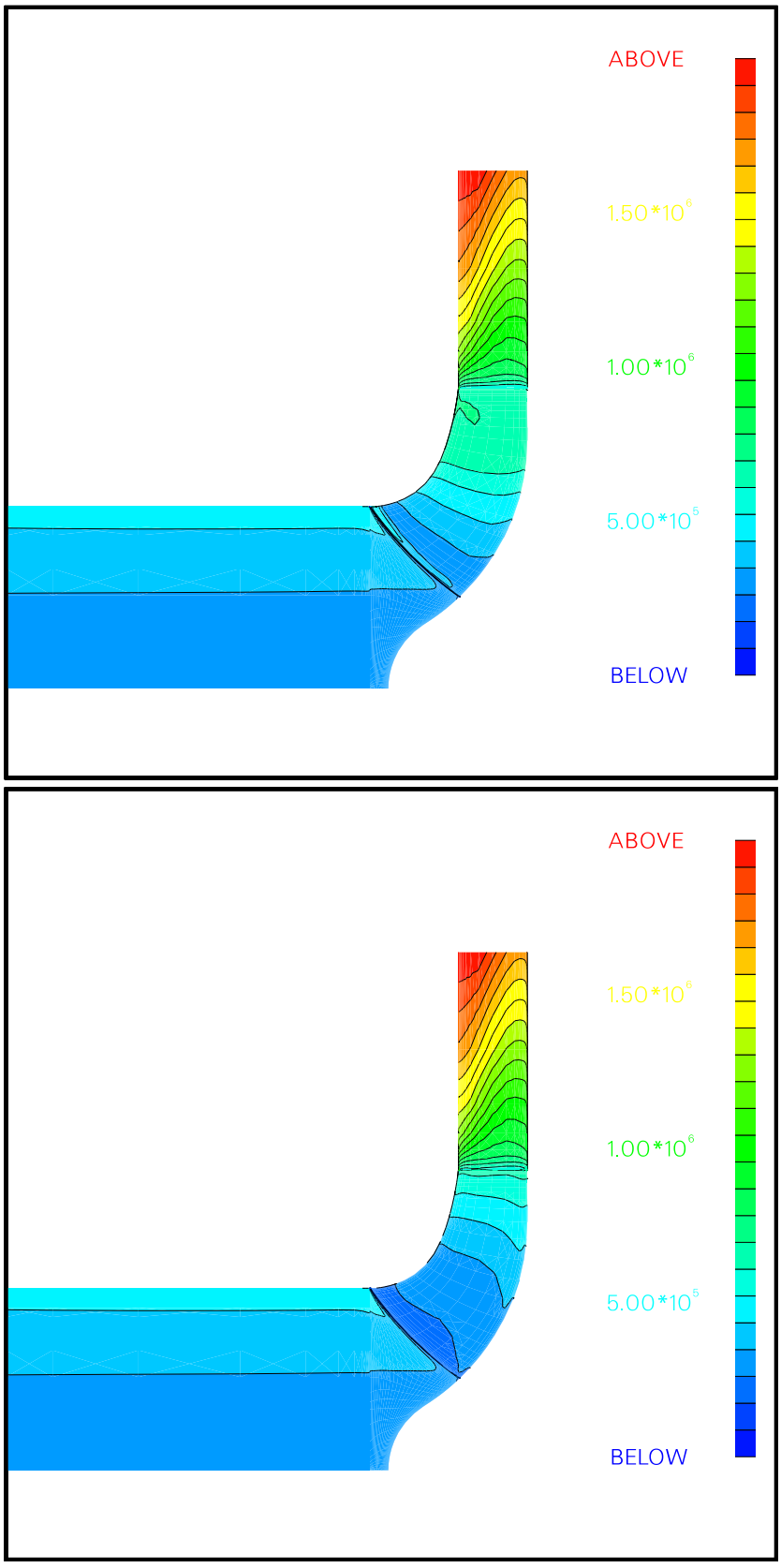

Fig. 30: Total pressure on the pressure and on the suction side (massflow 80 %, level 2)

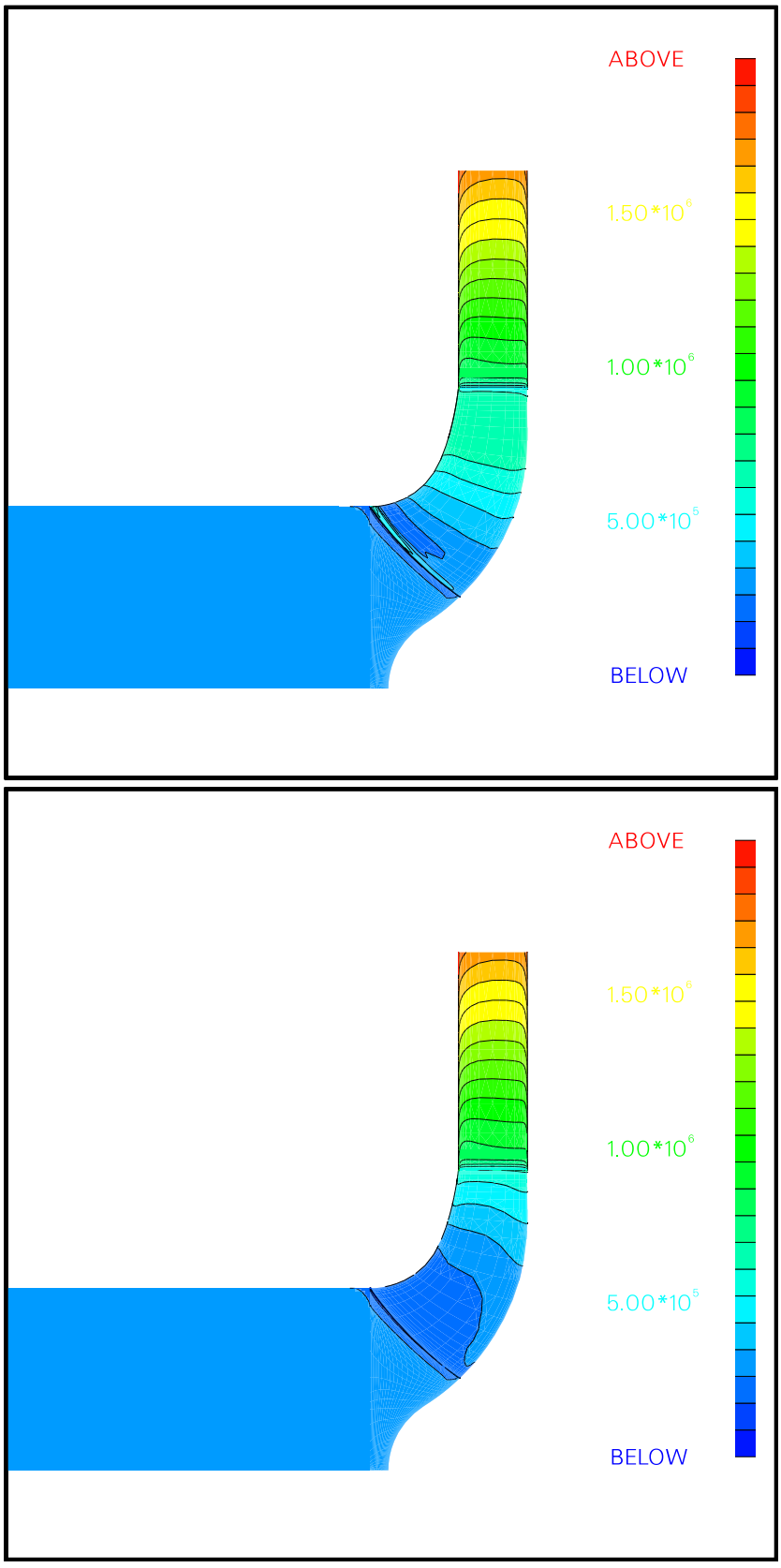

Fig. 31: Total pressure on the pressure and on the suction side (massflow 100 %, level 2)

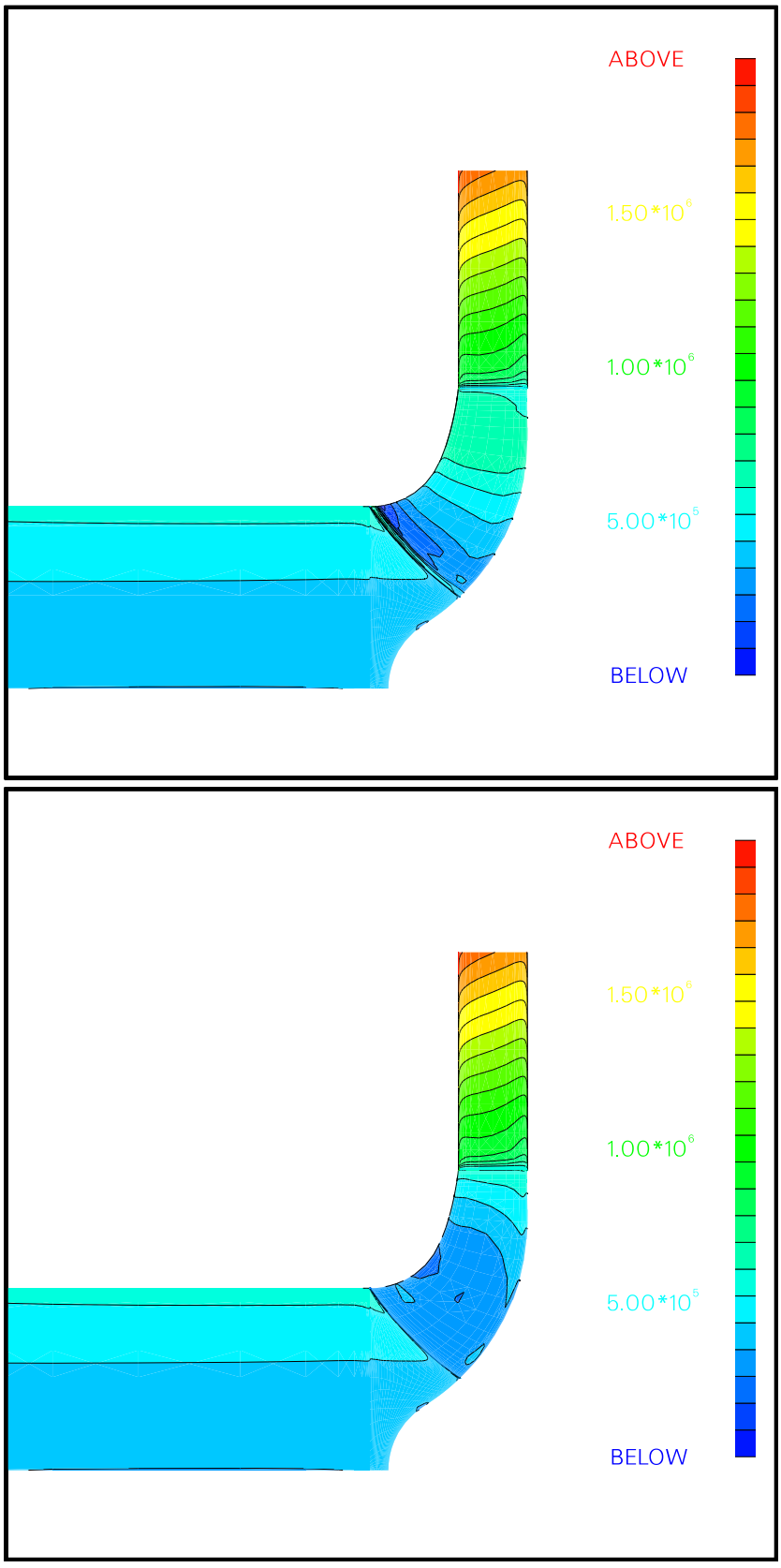

Fig. 32: Total pressure on the pressure and on the suction side (massflow 120 %, level 2)

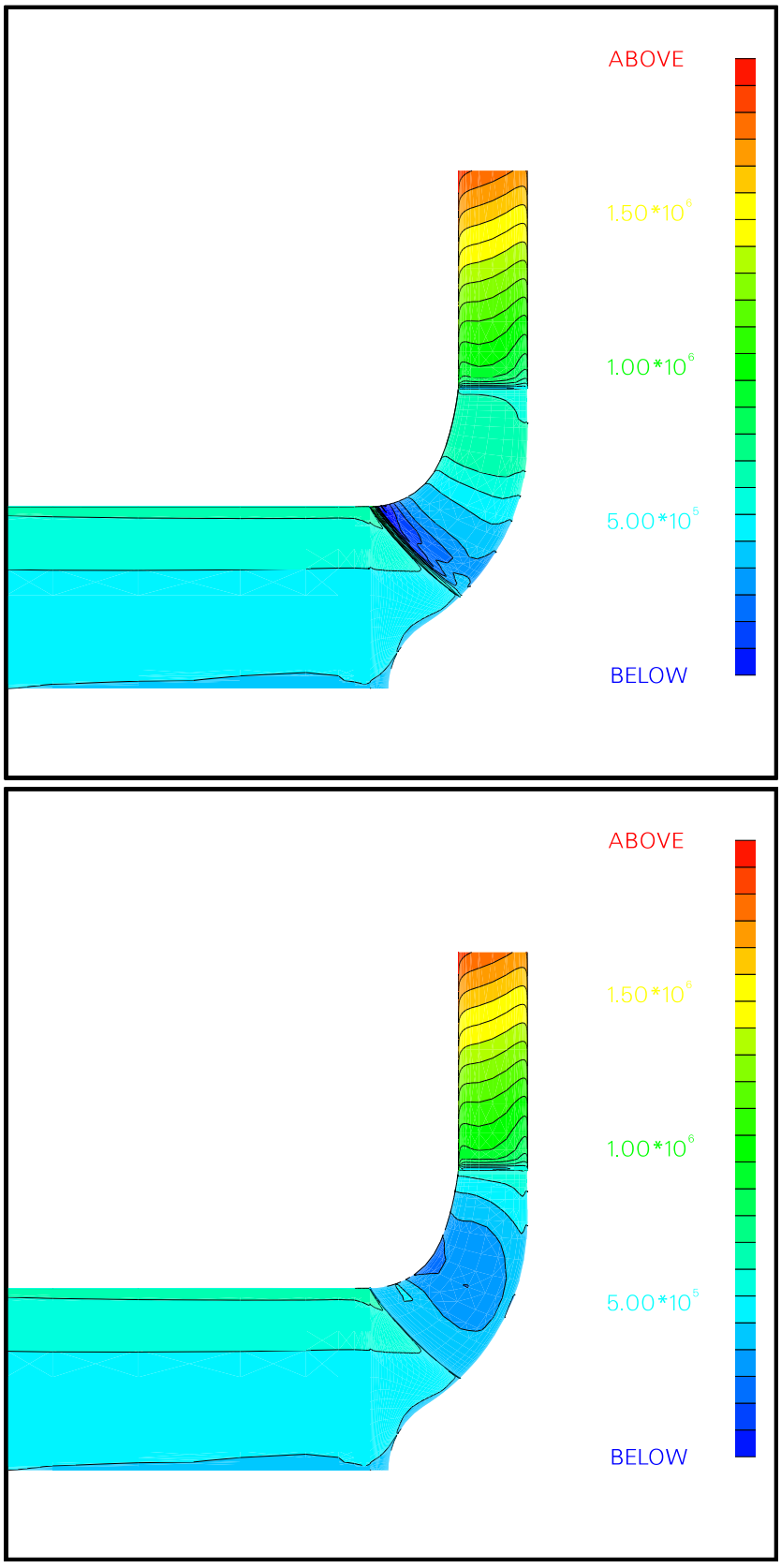

Fig. 33: Total pressure on the pressure and on the suction side (massflow 140 %, level 2)

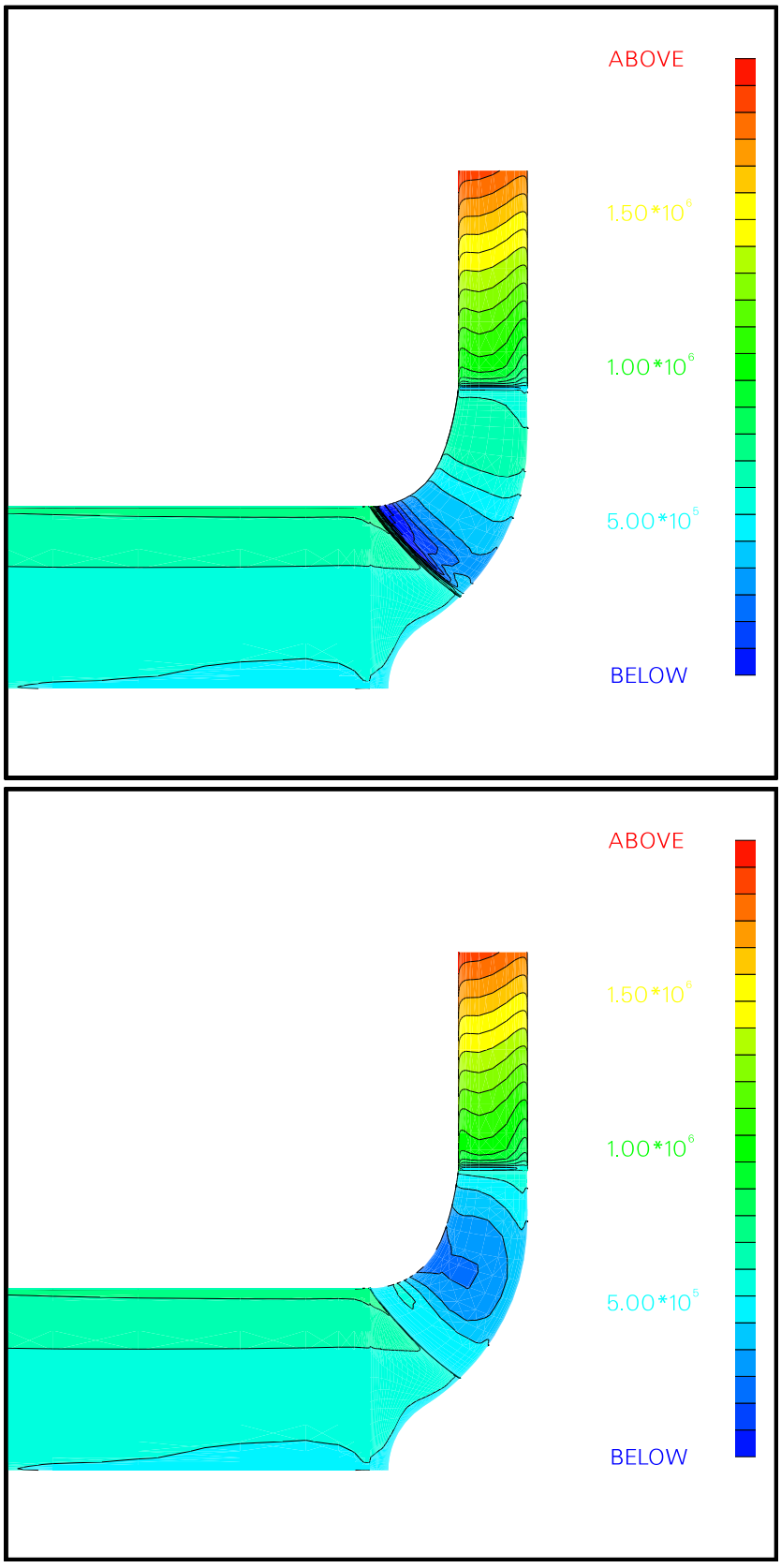

Fig. 34: Total pressure on the pressure and on the suction side (massflow 160 %, level 2)

Appendix F Static Pressure over the Blade

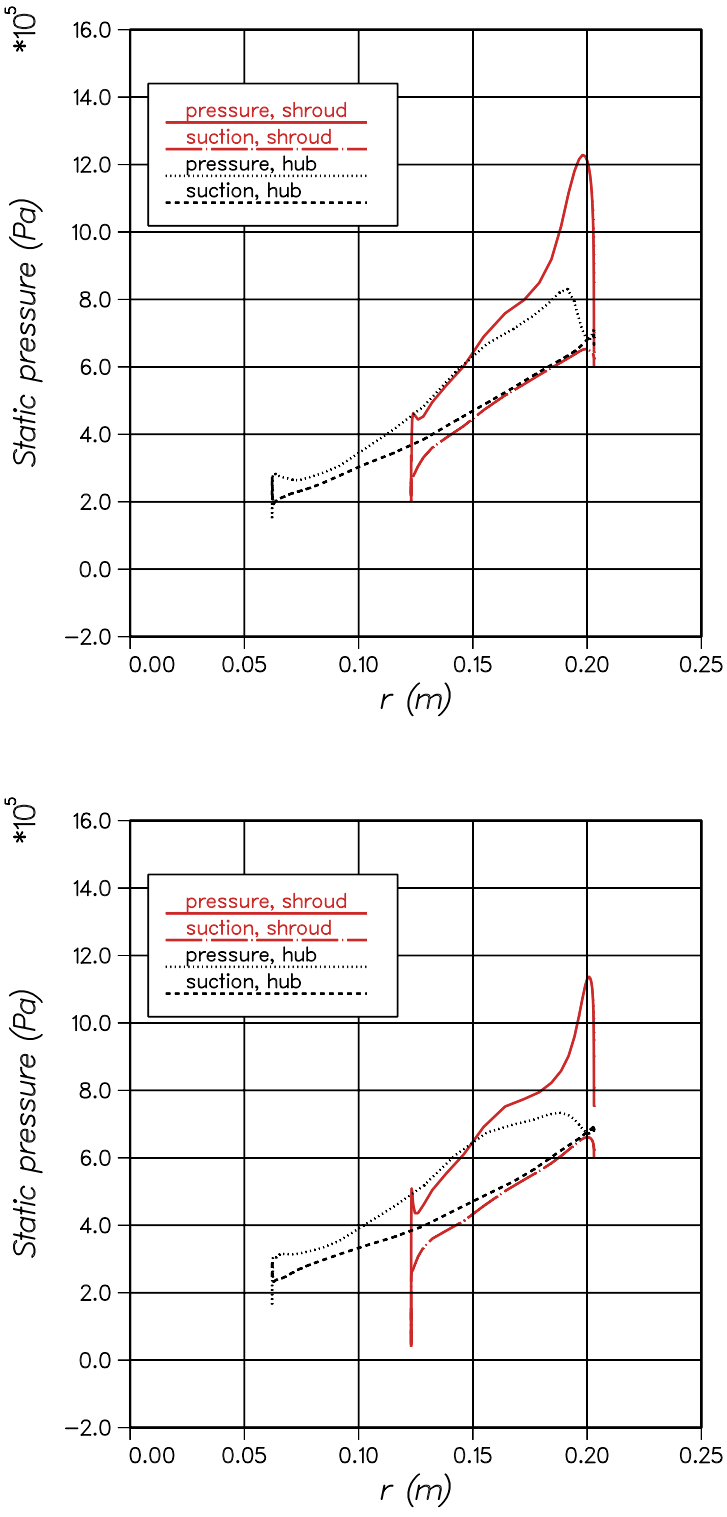

Fig. 35: Static pressure over the blade (massflows 20 % and 40 %, level 2)

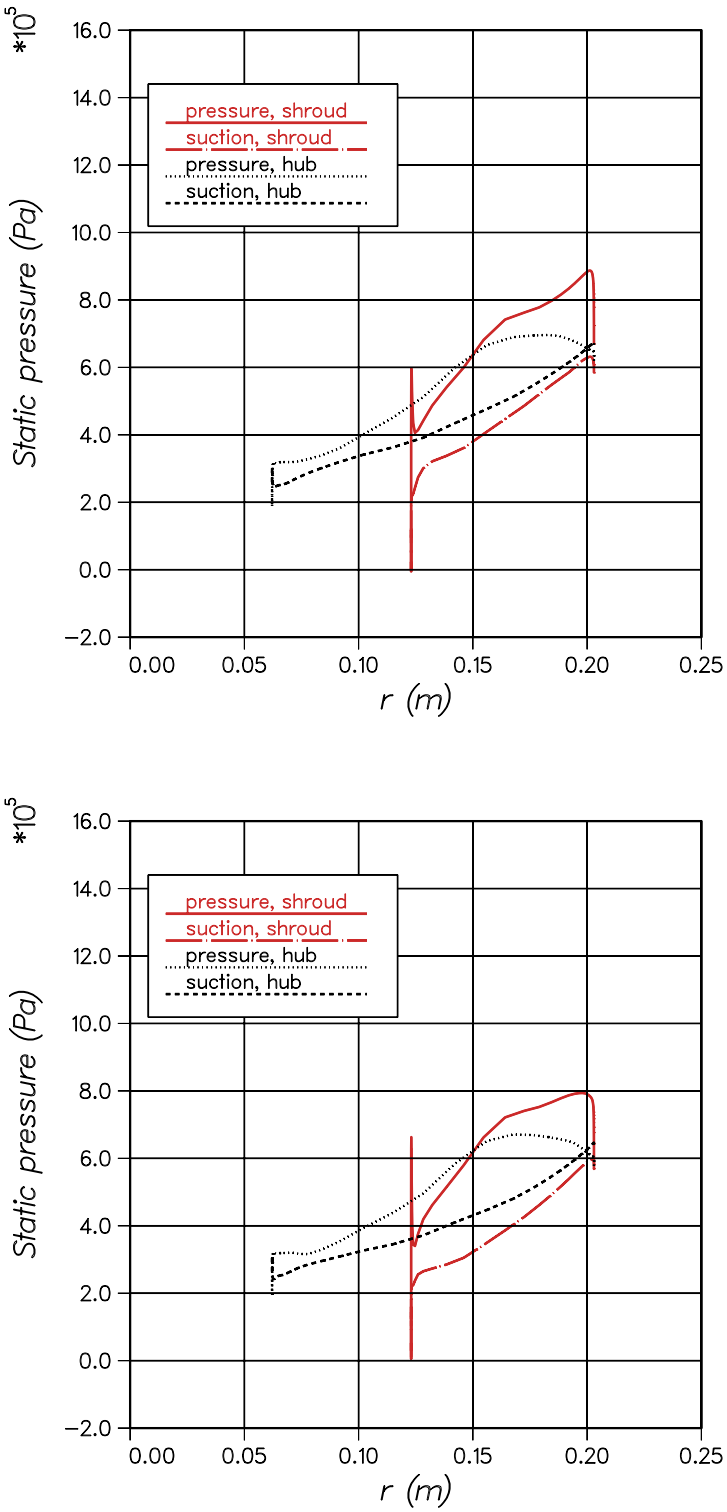

Fig. 36: Static pressure over the blade (massflows 60 % and 80 %, level 2)

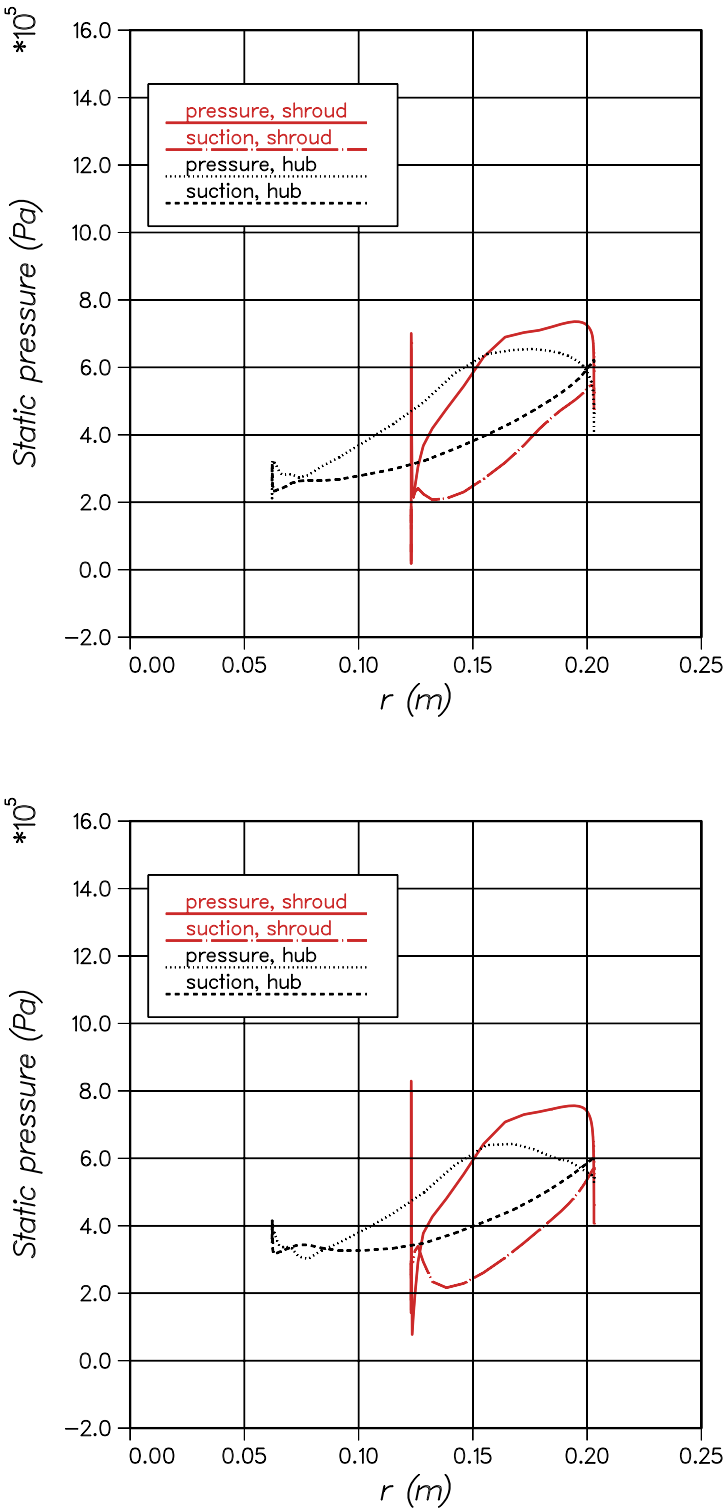

Fig. 37: Static pressure over the blade (massflows 100 % and 120 %, level 2)

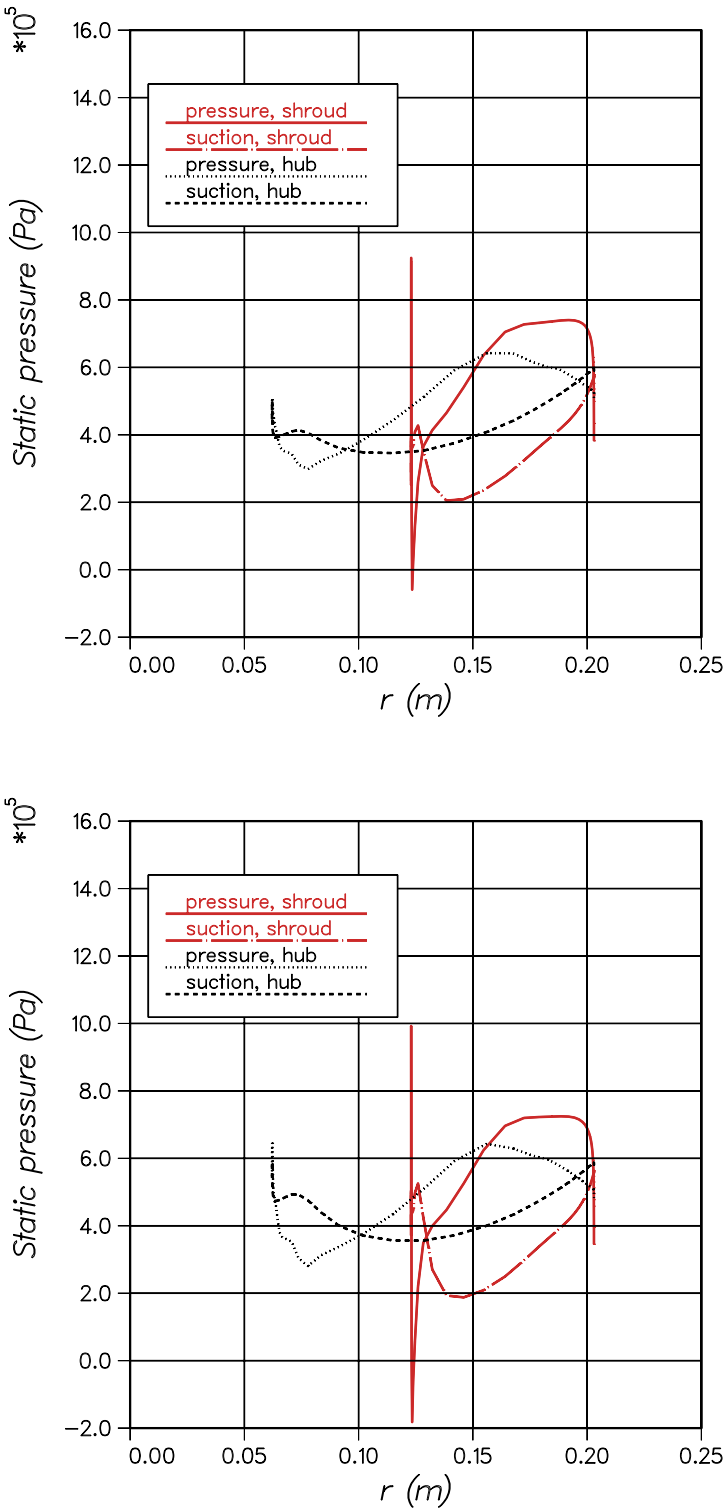

Fig. 38: Static pressure over the blade (massflows 140 % and 160 %, level 2)

Appendix G Total Pressure at Three Stations

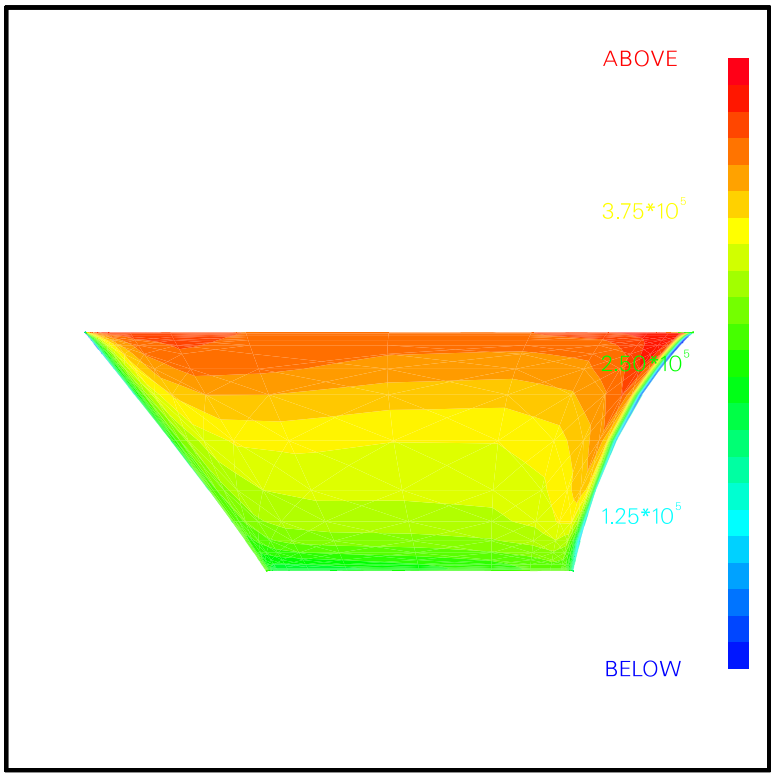

Fig. 39: Total pressure near the leading edge (at design point, level 2)

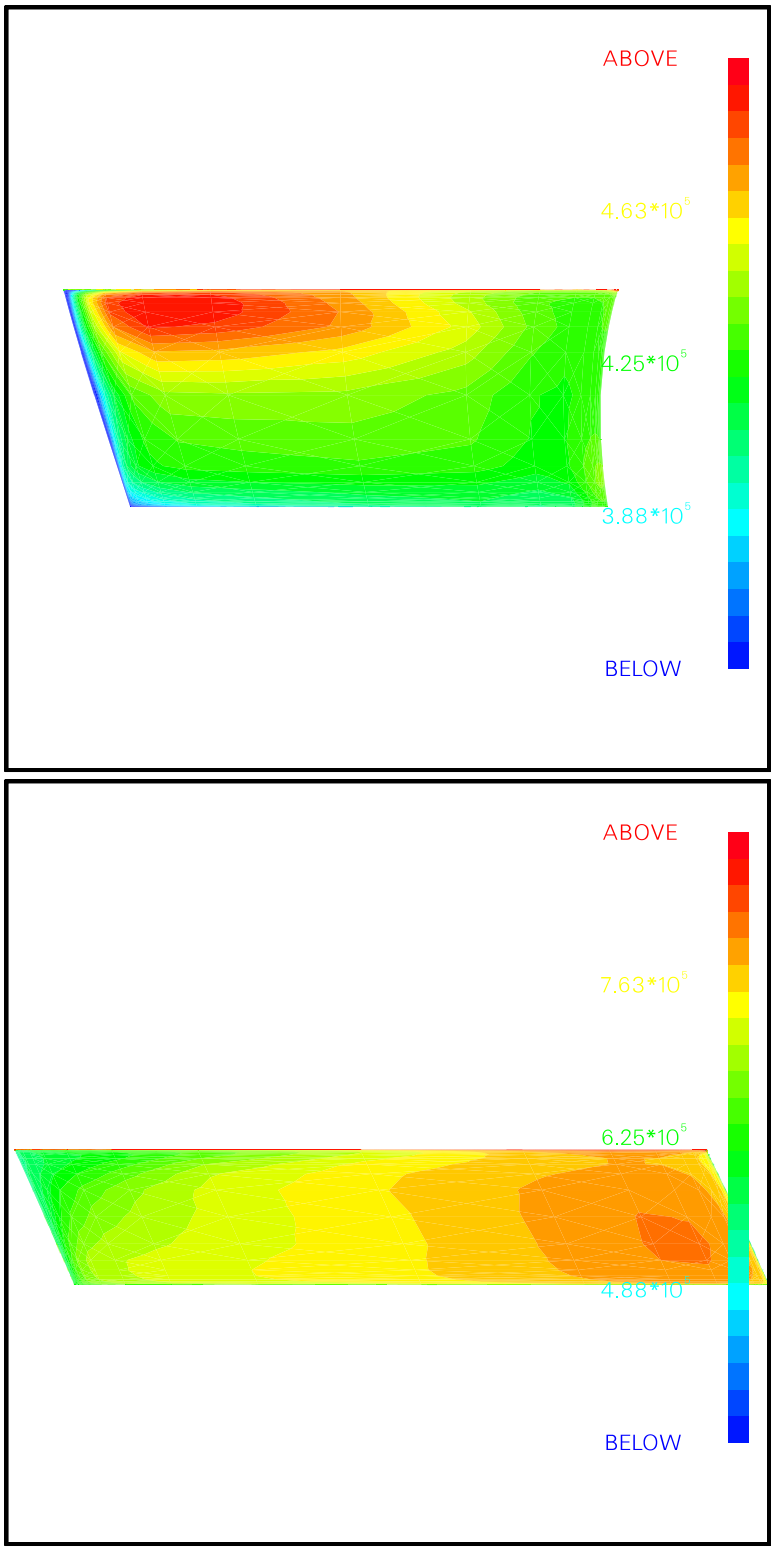

Fig. 40: Total pressure at 50 % chord and at the trailing edge (at design point, level 2)